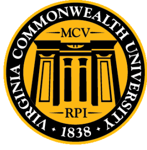

Virginia Commonwealth University
VCU Scholars Compass

Theses and Dissertations

Graduate School

2006

Determination of the Band Gap Bowing Parameter of A1xGa1-xN with Contactless Electroreflectance

Laura C. McGlinchey
Virginia Commonwealth University

Follow this and additional works at: https://scholarscompass.vcu.edu/etd

Part of the Physics Commons

© The Author

Downloaded from
https://scholarscompass.vcu.edu/etd/1002

This Thesis is brought to you for free and open access by the Graduate School at VCU Scholars Compass. It has been accepted for inclusion in Theses and Dissertations by an authorized administrator of VCU Scholars Compass. For more information, please contact libcompass@vcu.edu.

www.manaraa.com

DETERMINATION OF THE BAND GAP BOWING PARAMETER OF $Al_xGa_{1-x}N$ WITH CONTACTLESS ELECTROREFLECTANCE

A thesis submitted in partial fulfillment of the requirements for the degree of Master of Science in Physics at Virginia Commonwealth University.

by

LAURA C. MCGLINCHEY

B.S. in Mathematics, University of Richmond, 2000

B.A. in Physics, University of Richmond, 2000

M.S. in Physics, Virginia Commonwealth University, 2006

Director: Martin Muñoz
Assistant Professor, Department of Physics

Virginia Commonwealth University
Richmond, Virginia
May 2006

Acknowledgements

I would first like to thank Ms. Lindsay Hussey in whom I have found a talented colleague and wonderful friend. A classmate and confidante, her face will be the involuntary image of my time at VCU. Auditory remembrances will be allotted to my brilliant and patient teacher and advisor, Dr. Martin Muñoz. By challenging and encouraging me, he has produced a confident scientist.

Dr. Durig Lewis and Ms. Jennifer McLamb had hands in building the experimental "houses" and taking data that are a part of this thesis. I am grateful for their talents, assistance, and congeniality.

In the hopes that paragraph number does not imply importance, I'd like to thank my classmates, physics faculty and staff who have helped me and my brain to grow during these rapid past two years. Growth was significant! Attempting to list everyone would be futile, but know if you are reading this, your name belongs here.

I would be remiss if I failed to thank my parents, who adopted my twin sister and me from the other side of the world, and who have never once told us something was impossible. And to Magnus Åkesson, who successfully weathered my most stressful times by making me smile.

Last, and certainly not least, thanks be to God for making this world so wonderfully complex, yet at times so beautifully simple. The study of physics continues to convince me of His existence.

Table of Contents

Page

Acknowledgements ii

Table of Contents iii

List of Figures vi

List of Tables viii

Abstract ix

Chapter 1. Semiconductor Materials and Their Applications in Opto-electronics 1

1.1 Group III-Nitride Semiconductors 1

1.2 AlGaN Obstacles 2

Chapter 2. Optical Techniques for Band Gap Determination 3

2.1 Band Gap Determination Using Reflectivity 3

2.2 Band Gap Determination Using Photoluminescence 7

2.3 Band Gap Determination Using Modulation Spectroscopy 8

2.3.1 Instrumentation in Modulation Spectroscopy Techniques 8

Chapter 3. Electromodulation 11

3.1 Introduction 11

3.2 The Theory of Modulation Spectroscopy 12

3.2.1 The Dielectric Function and Optical Constants 12

3.2.2 The Dielectric Function and Band Structure 13

3.2.2.1 Classical Electromagnetic Fields....................14

3.2.2.2 Quantum Mechanically Described Electrons....................14

3.2.2.3 Fermi's Golden Rule....................15

3.2.2.4 Transition Probability and Optical Constants and the Dielectric Function....................18

3.2.2.5 Kramers-Kronig Relations....................18

3.2.3 Joint Density of States and Van Hove Singularities....................19

3.2.4 Lineshape Considerations....................22

3.2.4.1 Low-Field Regime....................23

Chapter 4. Experimental Procedures and Results....................28

4.1 Samples Growth....................28

4.2 Composition Determination by X-Ray Diffraction....................28

4.2.1 XRD Fundamentals....................29

4.2.2 XRD Concentration Calculation....................30

4.2.3 An Alternate Method....................34

4.3 Contactless Electroreflectance Experimental Setup....................34

4.4 Data Acquisition (DAQ)....................36

4.5 CER Results and Analysis....................38

Chapter 5. Conclusions....................46

References....................47

Appendix..49

A CER Experimental Equipment Settings..49

Vita..50

List of Figures

Page

Figure 1. Oblique reflection and transmission of a plane wave by an ambient(0)-film(1)-substrate(2) system with parallel-plane boundaries. d is the film thickness, ϕ_0 is the angle of incidence in the ambient and ϕ_1, ϕ_2 are the angles of refraction in the film and substrate, respectively. 3

Figure 2. Reflectivity spectra for an air/$Ga_{0.7}Al_{0.3}As$/GaAs for various film thicknesses. 6

Figure 3. Reflectivity spectra for an air/cubic GaN/GaAs heterostructure for various film thicknesses 6

Figure 4. Alloy fluctuations within the material will create corresponding energy band fluctuations 7

Figure 5. General schematic setup for experimental modulation spectroscopy. 9

Figure 6. Comparison of room-temperature reflectivity and electroreflectance of GaAs 11

Figure 7. Seraphin coefficients for Ge. Here, β_r corresponds to α and β_i to β. 22

Figure 8 Plane wave A A' A'' A''' is reflected by planes of atoms at B,B',B'',B''' Consider waves arriving at C. Path difference (marked by red lines) A'B'C-ABC=2dSin[θ]. When 2dSin[θ]=nλ all partial waves in C direction will be in phase. Hence, the interference is constructive. 29

Figure 9 (a) Diffraction schematic in k-space, where k is a wave vector. (b) Diagram of k, k', and Δk relation and orientation in a theta/2theta scan. 30

Figure 10. Hexagonal wurtzite structure and surface planes 31

Figure 11. A sample XRD logarithmic data spectra and fit with parameters. 32

Figure 12 CER set up. 35

Figure 13. CER sample holder. 36

Figure 14. Data acquisition menu in WinPR. 37

Figure 15 Experimental data from published works of Al composition in AlGaN versus energy band gap plotted as the deviation from zero bowing 38

Figure 16. CER spectra of $Al_xGa_{1-x}N$ for $0 < x < 0.48$. 39

Figure 17. Band structure of Wurtzite GaN. 40

Figure 18. Effect of Al concentration on the A excitonic transition of $Al_xGa_{1-x}N$. 42

Figure 19. Effect of Al concentration on the A excitonic transition of $Al_xGa_{1-x}N$. 43

Figure 20. Effect of Al concentration on the C excitonic transition of $Al_xGa_{1-x}N$ 44

List of Tables

Page

Table 1: Al Concentration XRD measurements and corresponding A-exciton

CER energy measurements. 41

Abstract

DETERMINATION OF THE BAND GAP BOWING PARAMETER OF $Al_xGa_{1-x}N$
WITH CONTACTLESS ELECTROREFLECTANCE

By Laura C. McGlinchey, M.S.

A thesis submitted in partial fulfillment of the requirements for the degree of Master of Science at Virginia Commonwealth University.

Virginia Commonwealth University, 2006

Major Director: Martin Muñoz
Assistant Professor, Department of Physics

Contactless electroreflectance (CER), a modulation spectroscopy (MS) technique, has been used to study the A and C exciton transitions in $Al_xGa_{1-x}N$ layers for a composition range of $0 \le x \le 0.48$ at room temperature. Taking the entire composition range ($0 \le x \le 1$) into account by incorporating a previously reported band gap energy for AlN, the dependence of the A-exciton transition on composition showed a downward bowing from linearity. A bowing parameter of b = 1.7 eV was found. Analysis of the lower composition range $0 \le x \le 0.48$ resulted in a linear fit, as did the trend for the detectable C exciton transitions. The slope of the linear trendlines for the A and C exciton were practically the same.

Chapter 1. Semiconductor materials and their application in opto-electronics.

1.1 Group III-Nitride Semiconductors

Group III-Nitride semiconductor materials have provided the impetus for exploding technological capabilities of the current time. Ultra-bright light emitting diodes (LEDs) are used for full-color signs, traffic lights, back illumination of hand-held displays, and even domestic lighting. LEDs and laser diodes (LDs) emitting in the ultraviolet (UV) region have important applications in the biological and chemical fields, namely, to monitor or catalyze chemical reactions, excite fluorescence in proteins, and detect molecules. UV lasers also have applications in the information technology field, particularly in Blu-Ray CD/DVD players and recorders [1], and high-density data storage [2] in general. The storage density of today's 1 Gb Digital Versatile Disk (DVD) is predicted to go up to about 40 Gb when blue lasers are used. Blue/violet lasers now dominate the Blu-Ray industry [3]. Currently, these devices are based on group III-Nitride compounds, and have emission wavelengths between 358 and 440 nm [4, 5].

In order to produce these UV devices it is necessary to use AlGaN barriers. The AlGaN alloy allows for a tunable direct energy gap between 3.42eV and 5.94eV, the respective band gaps of GaN and AlN. AlN itself is good in terms of its hardness, high thermal conductivity, and its resistance to high temperatures and caustic chemicals. The greater the concentration of Al, the higher the transition energy, and the shorter the emission wavelength.

1.2 AlGaN Obstacles

The main factor hampering AlGaN mass production is that materials quality remains poor at high concentrations of aluminum. Strain due to lattice mismatch between AlGaN and the substrates results in low crystalline quality. Non-uniform substrate temperatures during the growth process produce composition variations in the AlGaN layers containing high Al concentration. Consequently, Al composition tends to be difficult to determine, as it may vary across a sample. Defects and impurities concentrations are uncomfortably high, and manifest themselves in extensive absorption tails, which is bad in terms of losses within a device. Band gap measurement resolution proves difficult with eminent broadening of signals.

However, the promise of AlGaN far outweighs the hardships. Many scientists and engineers are progressing undoubtedly forward, so that we might see these materials dominating devices quite soon. In order to have an accurate design of the UV devices it is necessary to know the band gap of the AlGaN alloy as a function of the Al concentration. In this thesis, we have studies the band gap (Exciton A) of this alloy using contactless electroreflectance (CER).

Chapter 2. Optical Techniques for Band Gap Determination

For a fundamental understanding of bulk materials, heterostructures, and nanostructures, information on energy transitions and its relation to the band structure, is critical. Optical techniques provide non-invasive, accurate, and powerful methods to probe band structures and semiconductor properties in a variety of conditions. Many factors determine the appropriate technique for a specific study. Among the most popular for determining near band gap energies in AlGaN are optical reflection, absorption, transmission, photoluminescence (PL), and photoreflectance (PR). Missing from this list is contactless electroreflectance (CER), which is the basis of this thesis.

Reflectivity and other experimental optical techniques have their own unique advantages and drawbacks.

2.1 Band Gap Determination Using Reflectivity

Optical properties of semiconductors have been exploited for many decades in reflectivity measurements.

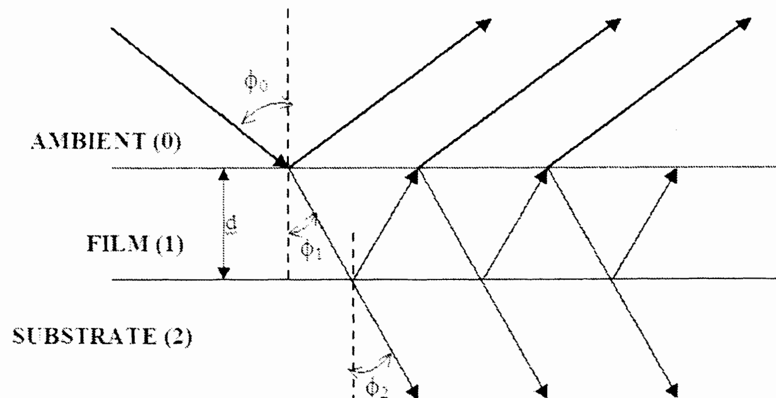

Figure 1. Oblique reflection and transmission of a plane wave by an ambient(0)-film(1)-substrate(2) system with parallel-plane boundaries. d is the film thickness, ϕ_0 is the angle of incidence in the ambient and ϕ_1, ϕ_2 are the angles of refraction in the film and substrate, respectively.[6]

In the three media (air/film/substrate) model illustrated in Figure 1, the total reflected amplitude of an optical plane wave is given by [6]

$$R = \frac{1}{2}\left(R_p + R_s\right) \tag{1}$$

where R_p and R_s are the complex amplitude reflection coefficients for the system for an incident wave linearly polarized either parallel (p) or perpendicular (s) to the plane of incidence. In terms of the interface Fresnel reflection coefficients (r_{01}, r_{12}), R_p and R_s are defined as:

$$\begin{aligned} R_p &= \frac{r_{01p} + r_{12p}e^{-i2\beta}}{1 + r_{01p}r_{12p}e^{-i2\beta}} \\ R_s &= \frac{r_{01s} + r_{12s}e^{-i2\beta}}{1 + r_{01s}r_{12s}e^{-i2\beta}} \end{aligned} \tag{2}$$

where the subscripts identify the ambient-film (0-1) and film-stubstrate (1-2) interfaces. In terms of the refractive indices, the Fresnel coefficients are:

$$\begin{aligned} r_{01p} &= \frac{n_1 \cos\phi_0 - n_0 \cos\phi_1}{n_1 \cos\phi_0 + n_0 \cos\phi_1} \\ r_{01s} &= \frac{n_0 \cos\phi_0 - n_1 \cos\phi_1}{n_0 \cos\phi_0 + n_1 \cos\phi_1} \\ r_{12p} &= \frac{n_2 \cos\phi_1 - n_1 \cos\phi_2}{n_2 \cos\phi_1 + n_1 \cos\phi_2} \\ r_{12s} &= \frac{n_1 \cos\phi_1 - n_2 \cos\phi_2}{n_1 \cos\phi_1 + n_2 \cos\phi_2} \end{aligned} \tag{3}$$

The phase change β results from multiple reflections of the wave inside the film as it travels through the film once from one boundary to the other. β is given by:

$$\beta = 2\pi \left(\frac{d}{\lambda} \right) \left(\tilde{n}_1^2 - \tilde{n}_0^2 \sin^2 \phi_0 \right)^{1/2} \tag{4}$$

where d is the film thickness, λ is the free-space wavelength, $\tilde{n}_i$ is the complex index of refraction, and ϕ_0 is the angle of refraction.

Typical reflectivity spectra show an oscillatory behavior below the band gap of the thin film and a damped oscillatory behavior above and around the band gap. From equation (4), it is evident that the period of these oscillations depends on the refractive index and thickness of the films under consideration.

Authors regularly assign the first or second minimum or maximum of the reflectivity spectra as the position of the band gap [7,8,24], without a reason for this assignment. Using equations (1) through (4), we performed simulations of the reflectivity for systems of air/$Ga_{0.7}Al_{0.3}As$/GaAs and air/cubic-GaN/GaAs for various film thicknesses. The dielectric function data was obtained from parameters established in references [9] and [10]. The results are shown below in Figures 2 and 3. The arrows indicate band gap assignments following the "rule" of the first minimum. The dashed vertical line indicates the true value of the band gap. We observe that the position of the minimum is dependent on layer thickness. Even the value of the minima directly below the band gap underestimates the true value. It is obvious this assignment of the band gap according to the position of the extrema in the reflectivity spectrum is wrong.

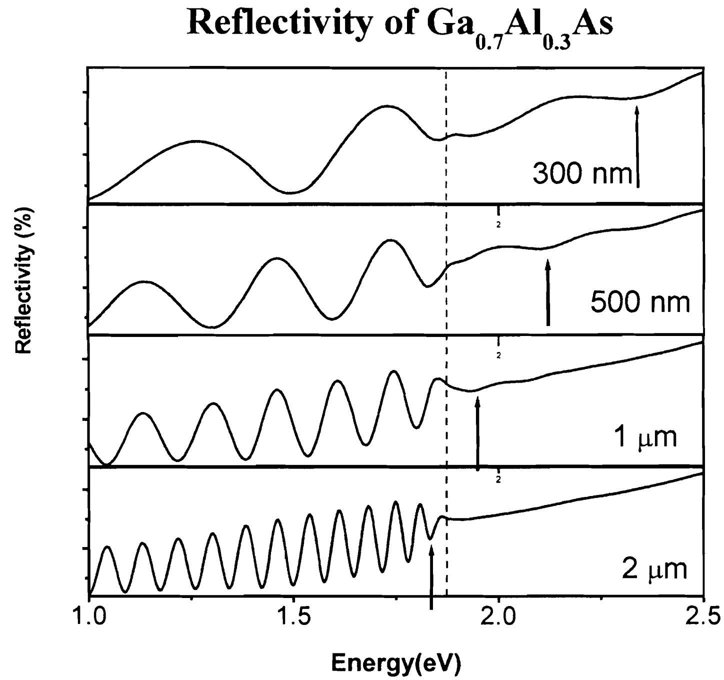

Figure 2. Reflectivity spectra for an air/$Ga_{0.7}Al_{0.3}As$/GaAs for various film thicknesses.

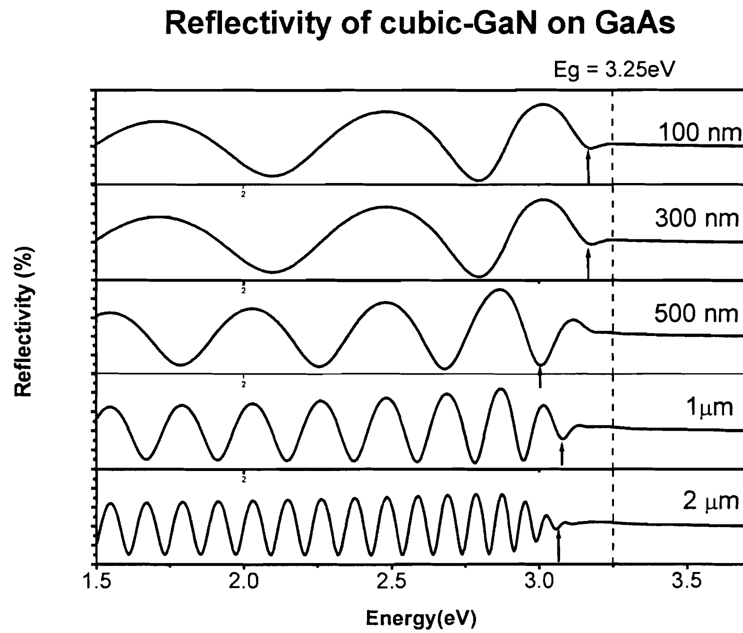

Figure 3. Reflectivity spectra for an air/cubic GaN/GaAs heterostructure for various film thicknesses

Apart from poor resolution, this procedure lacks a consistent model relating the band structure to the reflectivity spectrum.

2.2 Band Gap Determination Using Photoluminescence

There have been numerous experiments using Photoluminescence (PL) to determine the band gaps of semiconductor materials. The primary disadvantage of this technique is that PL underestimates the band gap because of its sensitivity to potential alloy fluctuations within the material. Figure 4 [11] illustrates this effect on the conduction and valence energy bands in GaN, and the preferential transition between the band extrema. This transition will then dominate the PL spectra, and underestimate the band gap energy.

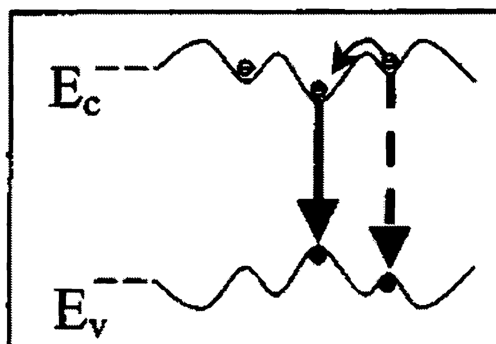

Figure 4. Alloy fluctuations within the material will create corresponding energy band fluctuations.

Room temperature PL spectra are characterized by broad bands, mostly due to temperature broadening. PL lines related to defects may mask or obscure band gap peaks. In addition, the determination of near band gap transitions based on PL experiments typically requires high-energy (short wavelength) lasers and cryogenic low temperatures.

2.3 Band Gap Determination Using Modulation spectroscopy

The underlying idea of Modulation Spectroscopy (MS) is to vary or modify some parameter in the experimental setup, and measure and interpret the resulting changes in the optical response, transmission or reflectivity, of the sample. Modulation is classified as external, where changes are applied to the sample; or internal, where changes are made to the measurement conditions. Examples of external modulation include varying an electric field (electromodulation), heat (thermomodulation), or stress (piezomodulation). Internal modulation may vary wavelength, slit opening, or polarization conditions.

2.3.1. Instrumentation in Modulation Spectroscopy Techniques

External modulation methods include photoreflectance (PR), electroreflectance (ER), contactless electroreflectlance (CER), thermoreflectance (THR) techniques, and peizoreflectance (PZR). All of the external MS techniques have a common fundamental set up, illustrated in Figure 5.

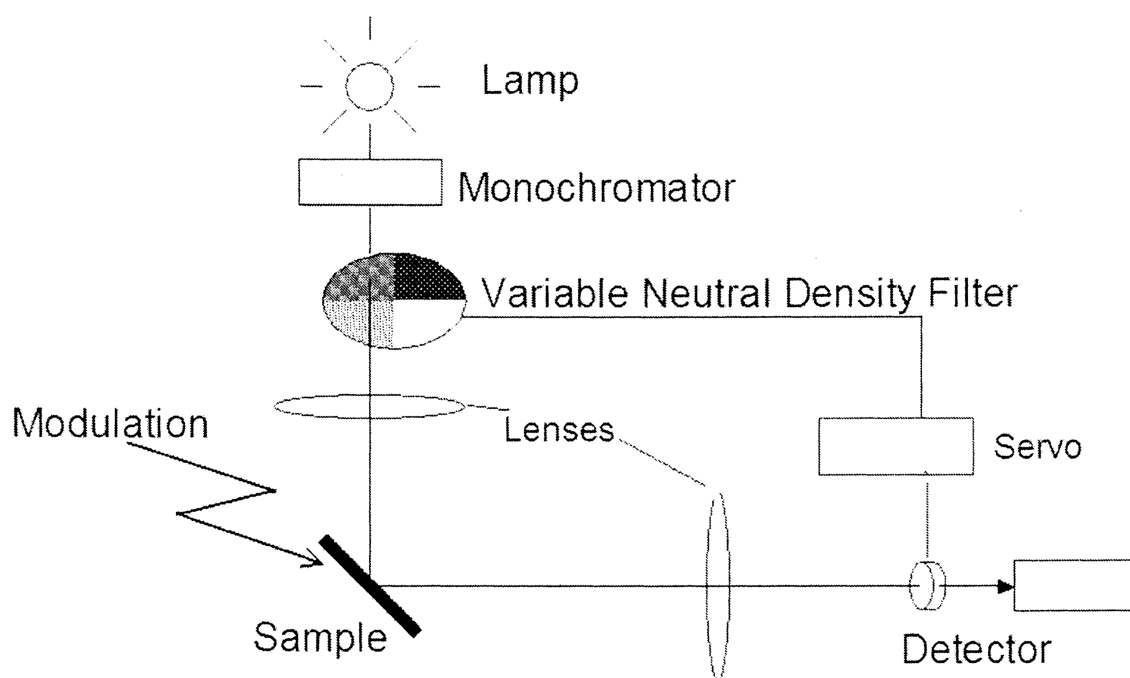

$$dc = I(\lambda)R(\lambda) = c$$

$$ac = I(\lambda)\Delta R(\lambda) = c\frac{\Delta R(\lambda)}{R(\lambda)}$$

Figure 5. General schematic setup for experimental modulation spectroscopy.

In the general MS setup, the sample is illuminated by a lamp. Monochromatic light is obtained by filtering the lamp's radiation using a monochromator. The variable neutral density filter (VNDF) keeps the light intensity constant through a logic loop with the servo, which is an electronics component, and the detector. The detector relays the direct current (dc) signal to the servo, which adjusts the VNDF in order to keep the monochromatic light intensity (dc signal) constant for all wavelengths, and therefore all energies, throughout the scan. The lenses in the set up serve to focus the light from the monochromator onto the sample, and collect reflected light from the sample into the detector. In addition to the monochromatic light, the sample is concurrently exposed to

some a.c. modulation such as an electric field, temperature, stress, etc. depending on the MS technique in use. This modulation produces small (a.c.) changes in the reflectivity for transitions that are detected using a lock-in amplifier. In this work, we modulated an electric field about the sample, which is detailed in the following chapter.

Chapter 3. Electromodulation

3.1 Introduction

Among MS techniques, electromodulation (EM) spectroscopy yields the sharpest structure. The resolution power and applicability of this technique to probe band structure in fabricated microstructures and thin films, in addition to bulk studies has been demonstrated. Specific transitions are identified in terms of energies and broadening functions. Even at room temperatures, transition energies may be obtained to within a few meV, and over a wide range of energies (0.5eV – 6eV). In addition, EM has the ability to analyze built in surface or interface electric fields due to above-band gap features, known as Franz-Keldysh Oscillations, present in the EM spectra. Figure 6 illustrates the outstanding advantages of EM: suppression of uninteresting background, and resolution of the transitions. The signals in the spectra are sharp, with derivative-like features, and measurements are accurate even at room temperature.

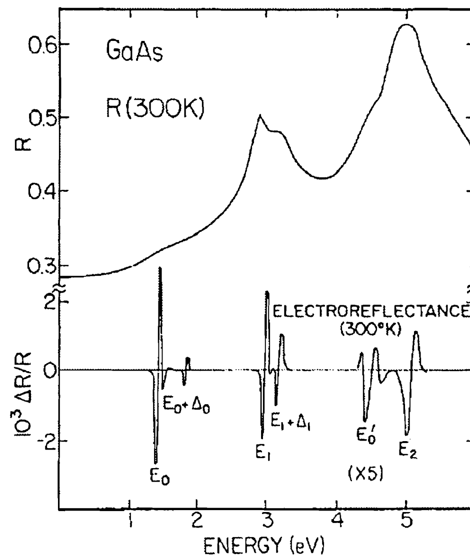

Figure 6. Comparison of room-temperature reflectivity and electroreflectance of GaAs [Pollak].

Electromodulation can be performed in three ways: photoreflectance (PR), electroreflectance (ER) and contactless electroreflectance (CER). PR uses a pump source (laser) to create an electric field by exciting carriers within the sample. The drawbacks of PR are that this method is limited to energies close to the excitation laser, typically ~3.8eV (HeCd laser) for nitride compounds. Additionally for wide band gap materials, PR spectra may include spurious modulated background signal due to strong photoluminescence (PL) from the sample, and/or (2) scattered light from the pump source. ER disadvantages lie in the contacts necessary for the technique. These contacts are not always transparent, a large concern for optical measurement. In addition, surface destruction and effects need to be considered.

CER eliminates many sources of error or difficulties present in other methods, as alluded to in the previous chapter. Among MS techniques, CER sidesteps the pitfalls present in PR and ER, while retaining the advantage of high resolution of modulation spectroscopy at room temperature. Despite these advantages, little work has been done on group III nitrides with this technique.

3.2 The Theory of Modulation Spectroscopy

The fundamental quantity that describes a material's optical response (reflectance or transmission) is the complex dielectric function.

3.2.1 The dielectric function and optical constants

The dielectric function ε is related to the index of refraction n, extinction coefficient κ, and absorption coefficient α. The dielectric as a function of frequency ω, and in terms of its real, $\varepsilon_1(\omega)$, and imaginary, $\varepsilon_2(\omega)$, parts is expressed as:

$$\varepsilon(\omega) = \varepsilon_1(\omega) + i\varepsilon_2(\omega) \tag{5}$$

For the complex refractive $\tilde{n}$ index defined as:

$$\tilde{n}(\omega) = n(\omega) + i\kappa(\omega) \tag{6}$$

the dielectric function and the complex refractive index are related by:

$$\varepsilon(\omega) = [\tilde{n}(\omega)]^2 \tag{7}$$

The real and imaginary parts of the dielectric function may be defined as:

$$\begin{aligned} \varepsilon_1 &= n^2 - \kappa^2 \\ \varepsilon_2 &= 2n\kappa \end{aligned} \tag{8}$$

The absorption coefficient can be expressed in terms of the above quantities:

$$\alpha = \frac{4\pi\kappa}{\lambda} = \frac{2\kappa\omega}{c} = \frac{\omega}{nc}\varepsilon_2 \tag{9}$$

where λ is the wavelength of light in vacuum. The absorption coefficient is related to the intensity of light passing spatially through a medium by:

$$I(\boldsymbol{r}) = I_0 \exp[-\alpha \boldsymbol{r}] \tag{10}$$

where $\boldsymbol{r}$ is the spatial distance in the direction of the light. We see a positive absorption coefficient corresponds to an exponential decay of light intensity. Equations (9) and (10) are used to relate the absorption coefficient to the imaginary part of the dielectric function in terms of transition probability in the following section.

3.2.2 The dielectric function and band structure

In order to obtain a relationship between the dielectric function and the band structure we will proceed through the following steps [12]:

1. Treat the electromagnetic field classically.

2. Use a quantum mechanical approach to describe the electrons using Bloch functions.
3. Use Fermi's Golden Rule to calculate the transition probability induced by a classical electromagnetic field.
4. With the transition probability, deduce the absorption coefficient α, and consequently, the imaginary part of dielectric function ε_2..
5. Use the Kramers-Kronig Relations to derive the imaginary part of the dielectric function ε_1.

These steps are described in detail in the following pages.

3.2.2.1 Classical electromagnetic fields

The electromagnetic field may be expressed in terms of a vector potential $A(\boldsymbol{r}, t)$, and a scalar potential $\Phi(\boldsymbol{r},t)$. For simplicity, we will choose the Coulomb gauge [13], where

$$\Phi = 0 \quad \text{and} \quad \nabla \cdot \mathbf{A} = 0 \tag{11}$$

The electric and magnetic fields then take the forms:

$$\boldsymbol{E} = -\frac{1}{c}\frac{\partial A}{\partial t} \qquad \text{and} \qquad \boldsymbol{B} = \nabla \times A \tag{12}$$

where c is the speed of light.

3.2.2.2 Quantum mechanically described electrons

Quantum Mechanics describes the effect of an electromagnetic field on the electronic states [14]. The electron momentum operator $\boldsymbol{p}$ is replaced to account for the field, as shown below.

$$p \rightarrow p + \frac{eA}{c}, \tag{13}$$

where e is electron charge, A is the vector potential associated with the electromagnetic field of the photon. The Hamiltonian of a particle in an electric field takes the form:

$$\mathcal{H} = \frac{1}{2m_0}\left(p + \frac{eA}{c}\right)^2 + V(r) \tag{14}$$

Where m_0 is the free electron mass. Expanding the first term of (14) yields:

$$\frac{1}{2m_0}p^2 + \frac{e}{2m_0c}A \cdot p + \frac{e}{2m_0c}p \cdot A + \frac{e^2}{c^2}A^2 \tag{15}$$

Since only linear optical effects will be considered here, the A^2 term is ignored. So the Hamiltonian describing the interaction between the electron and photon reduces to:

$$\mathcal{H}_{ep} = \frac{e}{m_0c}A \cdot p \tag{16}$$

This formula is referred to as the electron-radiation interaction Hamiltonian.

3.2.2.3 Fermi's Golden Rule

To calculate the dielectric function from the Hamiltonian of equation (16), we need to calculate the transition probability per unit volume for an electron in the valence band state $|v\rangle$ and the conduction band state $|c\rangle$. Assuming a small perturbation due to the electron-radiation interaction, or that A is small, we may apply time-dependent perturbation theory, in the form of Fermi's Golden Rule to determine this transition probability. We consider a perturbation of the form $V(r)\exp(\pm i\omega t)$, which induces a transition from the initial state to the final state. This time dependency gives rise to the delta function found in Fermi's Golden Rule [14], generally stated as:

$$\mathcal{P} = \frac{2\pi}{\hbar} \left\| \langle f | V | i \rangle \right\|^2 \delta(E_f - E_i \pm \hbar\omega) \tag{17}$$

where $\mathcal{P}$ is transition probability, $\langle f | V | i \rangle$ is the matrix element representing a particle interaction which causes transitions from an initial $|i\rangle$ to a final state $|f\rangle$, and $\delta(E_f - E_i \pm \hbar\omega)$ is a delta function involving energies of the final and initial states, which arises in the limit as time goes to infinity. In terms of the conduction and valence bands, a positive $\hbar\omega$ implies an electron in the valence band absorbs energy, and is excited into the conduction band (absorption). Negative $\hbar\omega$ corresponds to emission of a photon due to the reverse transition. Regardless, the delta function marks the transition as energy-conserving.

It is necessary to evaluate the matrix element $\langle f | V | i \rangle$ for a conduction band final state and a valence band initial state, and a potential defined by the electron-radiation Hamiltonian of equation (16). So the matrix element takes the form $\langle c | \mathcal{H}_{ep} | v \rangle$.

$$\left| \langle c | \mathcal{H}_{ep} | v \rangle \right|^2 = \left(\frac{e}{m_0 c} \right)^2 \left| \langle c | \boldsymbol{A} \cdot \boldsymbol{p} | v \rangle \right|^2 \tag{18}$$

If we write $\boldsymbol{A}$ as $A\hat{\boldsymbol{e}}$, where $\hat{\boldsymbol{e}}$ is a unit vector parallel to $\boldsymbol{A}$, in the direction of the polarization, the amplitude A can be expressed as:

$$A = -\frac{E}{2q} \left\{ \exp\left[i(\boldsymbol{q} \cdot \boldsymbol{r} - \omega t) \right] + c.c. \right\} \tag{19}$$

Where c.c stands for the complex conjugate.

For the electron valence and conduction band states written as Bloch functions:

$$\begin{aligned} |c\rangle &= u_{c,k_c}(\boldsymbol{r})\exp[i(\boldsymbol{k}_c \cdot \boldsymbol{r})] \\ |v\rangle &= u_{v,k_v}(\boldsymbol{r})\exp[i(\boldsymbol{k}_v \cdot \boldsymbol{r})] \end{aligned} \tag{20}$$

and combining (19) and (20), one can obtain:

$$\left\|\langle c|\boldsymbol{A}\cdot\boldsymbol{p}|v\rangle\right\|^2 = \frac{|E|^2}{4q^2}\left|\int u_{c,k_c}\exp\left[i\left(\boldsymbol{q}-\boldsymbol{k}_c\right)\cdot\boldsymbol{r}\right](\hat{\boldsymbol{e}}\cdot\boldsymbol{p})u_{v,k_v}\exp(i\boldsymbol{k}_v\cdot\boldsymbol{r})d\boldsymbol{r}\right|^2 \tag{21}$$

Evaluating the integral and utilizing the periodicity of the lattice, it is found

$$\int_{unit\,cell} u_{c,k_c}\exp\left[i\left(\boldsymbol{q}-\boldsymbol{k}_c+\boldsymbol{k}_v\right)\cdot\boldsymbol{r}\right]\boldsymbol{p}u_{v,k_v}d\boldsymbol{r}' = \int_{unit\,cell} u_{c,k_{v+q}}\boldsymbol{p}u_{v,k_v}d\boldsymbol{r}' \tag{22}$$

If we take the photon wavelength to be much larger than the lattice constants, one can use the electric dipole approximation, and consider only vertical transitions ($\boldsymbol{k}_c = \boldsymbol{k}_v = \boldsymbol{k}$). So the matrix element is now:

$$\left\|\langle c|\hat{\boldsymbol{e}}\cdot\boldsymbol{p}|v\rangle\right\|^2 = \left(\int_{unit\,cell} u_{c,k}(\hat{\boldsymbol{e}}\cdot\boldsymbol{p})u_{v,k_v}d\boldsymbol{r}'\right) = \left\|P_{cv}\right\|^2 \tag{23}$$

For further simplification, we will assume the remaining ($\hat{\boldsymbol{e}}\cdot\boldsymbol{p}$) in the matrix element is not strongly dependent on $\boldsymbol{k}$. We can then replace the momentum matrix element in (23) with a constant P_{cv}. Equation (18) becomes:

$$\left|\langle c|\mathcal{H}_{ep}|v\rangle\right|^2 = \left(\frac{e}{m_0 c}\right)^2 |A|^2 \left\|P_{cv}\right\|^2 \tag{24}$$

By substituting equations (19) and (24) into Fermi's Golden Rule (equation (17)), we arrive at the electric dipole transition probability $\mathcal{P}$ for photon absorption per unit time.

$$\mathcal{P} = \frac{2\pi}{\hbar}\left(\frac{e}{m_0 c}\right)^2 \left|\frac{E(\omega)}{2}\right|^2 \sum_{\boldsymbol{k}} \left\|P_{cv}\right\|^2 \delta\left(E_c(\boldsymbol{k}) - E_v(\boldsymbol{k}) - \hbar\omega\right) \tag{25}$$

3.2.2.4 Transition probability and optical constants and the dielectric function

Power lost by the field due to absorption in unit volume of the medium is related to the transition probability in equation (25):

$$\text{Power loss} = \mathcal{P}\,\hbar\omega \tag{26}$$

This power loss can be expressed in terms of the absorption coefficient α or the imaginary part of the dielectric function ε_2 since the rate of decrease in energy of the incident beam per unit volume is given by $-dI/dt$, for intensity I in equation (10), and absorption coefficient of equation (9).

$$-\frac{dI}{dt} = -\left(\frac{dI}{dx}\right)\left(\frac{dx}{dt}\right) = \alpha I\left(\frac{c}{n}\right) \tag{27}$$

$$= \frac{\varepsilon_2 \omega I}{n^2} \tag{28}$$

If we equate this rate of energy loss with the expression for power loss in equation (26), we obtain the imaginary part of the dielectric function in terms of the transition probability:

$$\varepsilon_2(\omega) = \left(\frac{2\pi e}{m\omega}\right)^2 \sum_{\boldsymbol{k}} \|P_{cv}\|^2 \delta[E_c(\boldsymbol{k}) - E_v(\boldsymbol{k}) - \hbar\omega] \tag{29}$$

3.2.2.5 Kramers-Kronig relations

The real part of the dielectric function is obtained through the Kramers-Kronig relations (KKRs) [12]:

$$\text{for } \varepsilon_2(\omega) = -\frac{2\omega}{\pi} \boldsymbol{P}\int_0^{\infty} \frac{\varepsilon_1(\omega')d\omega'}{\omega'^2 - \omega^2}$$

$$\varepsilon_1(\omega) - 1 = \frac{2}{\pi} \boldsymbol{P}\int_0^{\infty} \frac{\omega'\varepsilon_2(\omega')d\omega'}{\omega'^2 - \omega^2} \tag{30}$$

where $\boldsymbol{P}$ is the principal value of the integral. With this relationship between the imaginary and real parts of the dielectric function and equation (29), we arrive at an expression for ε_1.

$$\varepsilon_1(\omega) = 1 + \frac{4\pi e^2}{m}\left[\sum_k \left(\frac{2}{m\hbar\omega_{cv}}\right)\frac{\|P_{cv}\|^2}{\omega_{cv}^2 - \omega^2}\right] \tag{31}$$

Where $\hbar\omega_{cv} = E_c(\boldsymbol{k}) - E_v(\boldsymbol{k})$.

3.2.3 Joint density of states and Van Hove singularities

Instead of summing over the k-states, we will sum over states described by the energy. For this purpose, we use the well-known rule involving the density of states *D(E)*.[15]

$$\sum_k \rightarrow \int D(E)dE \tag{32}$$

The integration is over the interband energy difference $E_{cv} = E_c(k) - E_v(k)$, and the joint density of states $D_j(E_{cv})$ is given by [15]:

$$D_j(E_{cv}) = \frac{2}{(2\pi)^3} \int_{S(E_{cv})} \frac{dS_k}{\|\nabla_k E_{cv}\|} \tag{33}$$

where dS_k represents the surface in **k** space, for a constant energy surface *S*. By referencing equation (33), we see the most important contributions to the joint density of states comes from the singularities, when

$$\nabla_k (E_{cv}) = 0\,. \tag{34}$$

These so-called Van Hove singularities give rise to the structural features in the dielectric function. Equation (34) is fulfilled when

$$\nabla_k E_c(k) = \nabla_k E_v(k)\,. \tag{35}$$

This will occur when the bands are parallel. When $\nabla_k E_{cv}(k) = 0$, we may expand E_{cv} by a Taylor series, preserving only the quadratic terms:

$$E_{cv}(k) = E_g + \alpha_1 k_x^2 + \alpha_2 k_y^2 + \alpha_3 k_z^2 \tag{36}$$

where E_g is the band gap.

Van Hove singularities are classified by the number of negative coefficients α_i of equation (36). In three dimensions, they are labeled M_0, M_1, M_2, and M_3 for zero, one, two, and three negative coefficients, respectively. In direct band gap materials, the lowest energy absorption occurs at an M_0 critical point, called the fundamental band gap.

From the expression in equation (29) for the imaginary part of the dielectric function, and the equations (32) and (33), the results of equation (36) allow the calculation of dielectric function in terms of energy and a broadening parameter Γ. For M_0 critical points [12],

$$\varepsilon_2(E,\Gamma) \propto \frac{1}{E^2} \times \begin{cases} \left(E - E_g + i\Gamma\right)^{1/2} \; for\ 3D\ CPs \\ \ln\left(E - E_g + i\Gamma\right) \; for\ 2D\ CPs \\ \left(E - E_g + i\Gamma\right)^{-1/2} \; for\ 1D\ CPs \end{cases} \tag{37}$$

This relationship provides a more functional form in terms of experiment for both interpretation and line fitting considerations.

Experiment provides us with values of $\frac{\Delta R}{R}$. These normalized changes in reflectivity are related to the changes in the real and imaginary parts of the dielectric function ($\Delta\varepsilon_1$ and $\Delta\varepsilon_2$, respectively). Normal reflectivity R is defined in term of the complex index of refraction by:

$$R = \left| \frac{(\tilde{n}-1)}{(\tilde{n}+1)} \right|^2 \tag{38}$$

Since the changes in the reflectivity due to the perturbation are small (with intensity on the order of 10^{-6} to 10^{-4}), one considers the log scale. Taking the derivative of the log of R, and employing equations (6) and (7) results in the expression:

$$\frac{\Delta R}{R} = \mathrm{Re}\left[\frac{2n_a}{n(\varepsilon - \varepsilon_a)} \Delta\varepsilon \right] = \mathrm{Re}\left[(\alpha - i\beta)\Delta\varepsilon \right] \tag{39}$$

Separating the real and imaginary parts, the normalized changes in reflectivity are written in terms of the change in the dielectric function as:

$$\frac{\Delta R}{R} = \alpha(\varepsilon_1, \varepsilon_2)\Delta\varepsilon_1 + \beta(\varepsilon_1, \varepsilon_2)\Delta\varepsilon_2 \tag{40}$$

with the Seraphin coefficients α and β. The Seraphin coefficients can be written as:

$$\alpha = \frac{1}{R}\frac{\partial R}{\partial \varepsilon_1} \qquad \beta = \frac{1}{R}\frac{\partial R}{\partial \varepsilon_2} \tag{41}$$

and may be used to compare the real and imaginary contributions of the changes in the dielectric function at certain energies. Their typcial behavior is shown below in Figure 7.

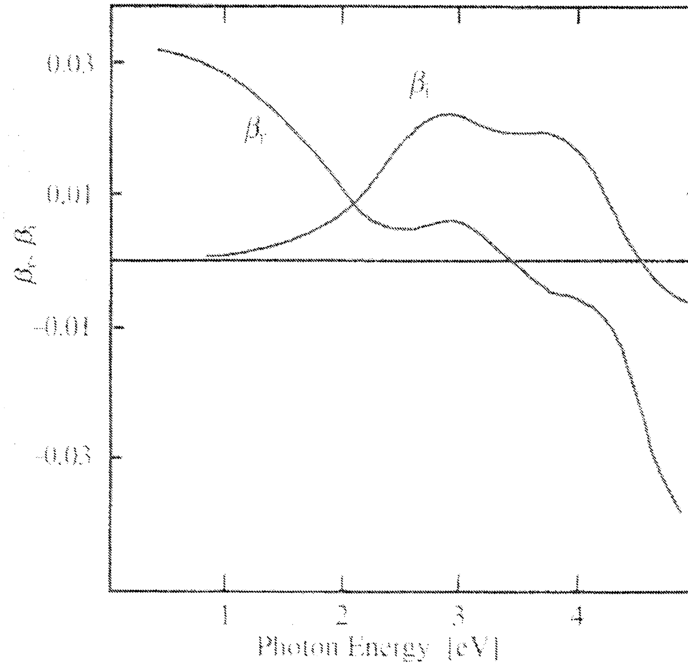

Figure 7. Seraphin coefficients for Ge. Here, β_r corresponds to α and β_i to β.

Near the fundamental gap in bulk materials, $\beta \approx 0$, so that $\frac{\Delta R}{R} \approx \alpha \Delta \varepsilon_1$. This changes for multi-layer structures where interference effects need to be considered.

Equation (40) provides the link between modulation spectroscopy experiment and the MS theory above. The following section delineates this connection in the theory behind the data analysis.

3.2.4 Lineshape Considerations

In electromodulation, there are three categories of classification: low-, mid- and high-field regimes. These are assigned depending on the relative strengths of the characteristic electrooptical ($\hbar\Theta$) energy defined as:

$$(\hbar\Theta) = \left(\frac{(e\hbar F)^2}{2\mu_{\|}} \right)^{1/3} \tag{42}$$

for the electric field F, reduced interband effective mass in the direction of the field $\mu_{\parallel}$ (see equation (51) below), and the charge of an electron e.

$$\begin{array}{ll} |\hbar\Theta| \leq \Gamma & \text{low field} \\ |\hbar\Theta| \geq \Gamma,\ eFa_0 \ll E_g & \text{intermediate field} \\ |\hbar\Theta| \geq \Gamma,\ eFa_0 \approx E_g & \text{high field} \end{array} \qquad (43)$$

Γ is the broadening parameter of the MS signal, and a_0 is the lattice constant. For the intermediate and high field, eFa_0 represent the energy gained by an electron due to the electric field perturbation as it is accelerated across the distance of one unit cell. The high field can destroy the band structure, in that an external electric field can break the translational symmetry of the crystal, which results in the acceleration of unbound electrons and holes. This will alter the Hamiltonian in the time-dependent Schrödinger equation. The results for an electron in a crystal subjected to a uniform electric field are presented below for the low-field regime.

3.2.4.1 Low-Field Regime

The main effect of an electric field on a periodic system is to change the wave vector from $\boldsymbol{k}$ to $\boldsymbol{k} - \frac{eFt}{\hbar}$ [15]. According to the semi-classical approach, the expression for the wave vector's rate of change is

$$\frac{d\mathbf{k}}{dt} = \frac{-eF}{\hbar} \quad \Rightarrow \mathbf{k}(t) = \mathbf{k}(0) - \frac{eFt}{\hbar} \qquad (44)$$

We will use this result in equation (29) for an expression of the imaginary dielectric function in a low electric field. For cv representing the states in the conduction and valence bands, and BZ an abbreviation for the brillouin zone, we can substitute

$$\sum_{k} \rightarrow \sum_{cv} \int_{BZ} d\boldsymbol{k} \tag{45}$$

and equations (44) into equation (29), taking broadening into account. The dielectric is now a function of the frequency, the electric field, and the broadening parameter.

$$\varepsilon_2(\omega, \boldsymbol{F}, \Gamma) = \left(\frac{2\pi e}{m\omega}\right)^2 \sum_{c,v} \int_{BZ} d\,\mathbf{k} \left\|P_{cv}\right\|^2 \delta[E_{cv}(\mathbf{k} - \frac{e\boldsymbol{F}t}{\hbar}) + i\Gamma - \hbar\omega] \tag{46}$$

Using the delta function in the form [16]:

$$\delta(x) = \frac{1}{2\pi} \int_{-\infty}^{\infty} \exp\{-ikx\} dk \tag{47}$$

equation (46) may be written:

$$\varepsilon_2(\omega, \boldsymbol{F}, \Gamma) = \left(\frac{2\pi e}{m\omega}\right)^2 \sum_{c,v} \int_{BZ} d\,\mathbf{k} \left\|P_{cv}\right\|^2 \frac{1}{2\pi} \int dt \exp\left\{-i[E_{cv}(\mathbf{k} - \frac{e\boldsymbol{F}t}{\hbar}) + i\Gamma - \hbar\omega]t\right\} \tag{48}$$

In terms of photon energy, $E = \hbar\omega$, (48) can be rewritten

$$\varepsilon_2(E, \boldsymbol{F}, \Gamma) = \left(\frac{2\pi e\hbar}{mE}\right)^2 \sum_{c,v} \int_{BZ} d\,\mathbf{k} \left\|P_{cv}\right\|^2 \frac{1}{2\pi} \int dt \exp\left\{-i[E_{cv}(\mathbf{k} - \frac{e\boldsymbol{F}t}{\hbar}) + i\Gamma - E]t\right\} \tag{49}$$

If we expand the E_{cv} of (49) in a Taylor series in terms of the field, and consider up to the second order term, the expansion takes the form:

$$[E_{cv}(\mathbf{k} - \frac{e\boldsymbol{F}t}{\hbar})]t \approx E_{cv}(\mathbf{k})t + \hbar\left(\Theta t\right)^3 \tag{50}$$

where $\hbar\Theta$ is defined by from equation (42) . Note the second term of the expansion is zero since we are considering E_{cv} around critical points. The effective mass tensor $\mu_{\|}$, which effects the curvature of the energy surface, is defined as [15]

$$\left[\frac{1}{m_c^*(\boldsymbol{k})}\right]_{ij} = \frac{1}{\hbar^2}\frac{\partial^2 E_c(\boldsymbol{k})}{\partial k_i \partial k_j}, \text{ for electrons in the conduction band or}$$

$$\left[\frac{1}{m_v^*(\boldsymbol{k})}\right]_{ij} = -\frac{1}{\hbar^2}\frac{\partial^2 E_v(\boldsymbol{k})}{\partial k_i \partial k_j}, \text{ for holes in the valence band} \tag{51}$$

$$\text{where } \frac{1}{\mu_{\parallel}} = \frac{1}{m_c^*} + \frac{1}{m_v^*}$$

This explains the form of the third term of the expansion, the second term of the right hand side of equation (50). Substituting this result into equation (49):

$$\varepsilon_2(E,F,\Gamma) = \left(\frac{2\pi e\hbar}{mE}\right)^2 \sum_{c,v} \int_{BZ} d\,\mathbf{k} \left\|P_{cv}\right\|^2 \frac{1}{2\pi} \int dt \exp\left\{-i[E_{cv}(\mathbf{k}) + i\Gamma - E]t - i\hbar\left(\Theta t\right)^3\right\} \tag{52}$$

Since the field is small, we can expand the exponential factor:

$$\exp\left\{-i\hbar\left(\Theta t\right)^3\right\} \approx 1 - i\hbar\left(\Theta t\right)^3 \tag{53}$$

Also, for the field $\boldsymbol{F} = 0$, equation (49) takes the form:

$$\varepsilon_2(E,0,\Gamma) = \left(\frac{2\pi e\hbar}{mE}\right)^2 \sum_{c,v} \int_{BZ} d\,\mathbf{k} \left\|P_{cv}\right\|^2 \frac{1}{2\pi} \int dt \exp\left\{-i[E_{cv}(\mathbf{k}) + i\Gamma - E]t\right\} \tag{54}$$

Using (53) and (54), equation (52) becomes:

$$\begin{gathered} \varepsilon_2(E,F,\Gamma) = \varepsilon_2(E,0,\Gamma) + \\ \left(\frac{2\pi e\hbar}{mE}\right)^2 \sum_{c,v} \int_{BZ} d\,\mathbf{k} \left\|P_{cv}\right\|^2 \frac{1}{2\pi} \int dt \exp\left\{-i[E_{cv}(\mathbf{k}) + i\Gamma - E]t\right\}\left[-i\hbar\left(\Theta t\right)^3\right] \end{gathered} \tag{55}$$

If we take the third partial derivative of equation (54) with respect to energy, we can rewrite (55):

$$\varepsilon_2(E,F,\Gamma) = \varepsilon_2(E,0,\Gamma) + \frac{\left(\hbar\Theta\right)^3}{12E^2}\frac{\partial^3}{\partial E^3}\left[E^2 \varepsilon_2(E,0,\Gamma)\right]. \tag{56}$$

Note that ε_1 is now obtainable through the Kramers-Kronig relation. Equation (56) implies the change in the complex dielectric function in the presence of a weak electric field is given by:

$$\Delta\varepsilon = \varepsilon(E,F,\Gamma) - \varepsilon(E,0,\Gamma) = \frac{(\hbar\Theta)^3}{12E^2}\left[\left(\frac{\partial^3}{\partial E^3}\right)E^2\varepsilon(E,0,\Gamma)\right] \tag{57}$$

For Lorentzian broadening of equation (57),

$$\Delta\varepsilon(E,F,\Gamma) = \Delta\varepsilon(E+i\Gamma,F,0) \tag{58}$$

and equations (40) and (57) can be written simply as

$$\frac{\Delta R}{R} \propto (\hbar\Theta)^3 \operatorname{Re}\left[e^{i\theta}\left(E - E_g + i\Gamma\right)^{-m}\right] \tag{59}$$

where θ is the phase angle, and *m* depends on the critical point type. The phase angle is a result of the mixture between the real and imaginary parts of the dielectric function as well as the non-uniform electric fields and interference and electron-hole interaction effects. In the case of an M_0 three dimensional critical point without excitonic effects, the dielectric function goes as the square root of the energy: $\varepsilon \,\alpha \sqrt{E-E_g}$. A third derivative would yield $m = 5/2$ in equation (59). This process may be applied to M_0 critical points in one and two dimensions by setting set *m* accordingly.

$$m = \begin{cases} 5/2 \; for \; 3D \; CPs \\ 3 \quad for \; 2D \; CPs \\ 7/2 \; for \; 1D \; CPs \end{cases} \tag{60}$$

In the case of bound states and excitons, the lineshape equations following (59) may be applied if we consider $m = 2$. The modulating field, in this case, acts to alter the exciton binding energy. Details may be found in reference [17].

In summary, lineshapes in CER are fit to (59), and consider (60) as such:

$$\frac{\Delta R}{R} \propto (\hbar\Theta)^3 \operatorname{Re}\left[e^{i\theta}\left(E - E_g + i\Gamma\right)^{-m}\right] \quad \text{for } m = \begin{cases} 5/2 \ \mathit{for}\ 3D\ \mathit{CPs} \\ 3 \quad \mathit{for}\ 2D\ \mathit{CPs} \\ 7/2 \ \mathit{for}\ 1D\ \mathit{CPs} \\ 2\ \mathit{for}\ \text{Excitons} \end{cases} \tag{61}$$

Chapter 4. Experimental Procedures and Results

4.1 Samples Growth

In molecular beam epitaxy (MBE) growth, GaN surface morphology is very sensitive to Ga coverage. A smooth surface can only be observed under Ga rich conditions. In the case of AlGaN growth, the surface morphology can also be controlled by Ga and Al coverage: with careful adjustments to their flux, an atomically smooth surface can be achieved. The structure of the sample consisted of a 430 μm sapphire substrate, with a 2 μm GaN buffer layer grown by metal-organic chemical vapor deposition (MOCVD), and finally an MBE-grown AlGaN layer. The MBE system used to grow the samples has four Knudsen cells, two Ga and two Al, and one nitrogen RF plasma source. For a smooth surface, the growth rates were fixed to about 200 nm/hour, and limited by the nitrogen source. The Al concentration is controlled by the Al flux. Typical substrate growth temperatures for AlGaN range from 700°C to 750°C. The samples in this study were grown in the lab of Dr. Hadis Morkoç at Virginia Commonwealth University.

4.2 Composition Determination by X-Ray Diffraction

XRD is of great use in solid state physics [18] in that it provides information about lattice spacing. The technique is straightforward, and relatively fast. Altering angles of the sample allow for observation and analysis of the crystal structure in various directions, most useful in determining or verifying lattice constants.

Coupled with Vergard's Law - that the lattice constant and alloy concentration are linearly related - the ternary alloy composition in semiconductor materials was determined. It should be noted here that due to the difficulty in growing high Al concentration AlGaN, alloy composition may fluctuate across the surface of these samples. Strain due to lattice mismatch with the substrate, and clustering of AlN and GaN are probable causes.

4.2.1 XRD Fundamental Theory

Diffraction of waves by a crystal is governed by Bragg's Law:

$$2d\sin\theta = n\lambda \tag{62}$$

where d is the lattice spacing, θ is the angle of diffraction, n is the order of diffraction, and λ is the wavelength of the X-ray. The law states that diffraction occurs only when the path difference between sets of incident and reflected plane waves differs by an integer number of wavelengths, shown below in Figure 8. When this occurs, all reflected waves will be in phase, and their interference will be constructive.

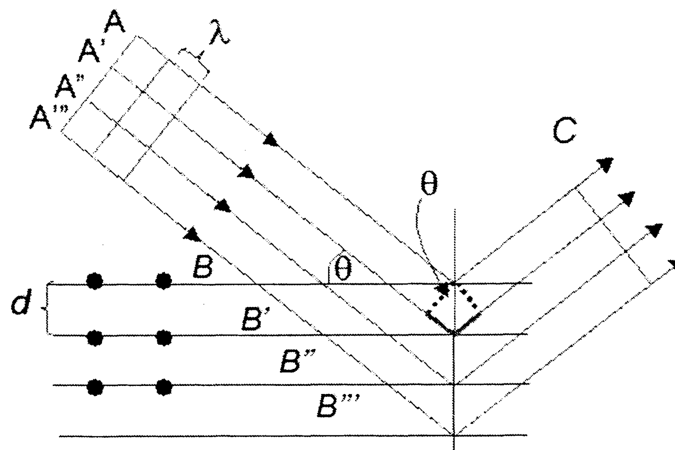

Figure 8 Plane wave A A' A'' A''' is reflected by planes of atoms at B,B',B'',B''' Consider waves arriving at C. Path difference $A'B'C-ABC=2d\text{Sin}[\theta]$. When $2d\text{Sin}[\theta]=n\lambda$ all partial waves in C direction will be in phase. Hence, the interference is constructive.

The XRD technique used here is the $\theta/2\theta$, or Gonio, scan. In this scan, the sample and detector are rotated with respect to the X-ray beam. In effect, the magnitude of Δk is varied while maintaining its normal incidence to sample. Figure 9 illustrates a schematic for diffraction in k-space, as well as a diagram of the sample orientation during the $\theta/2\theta$ scan.

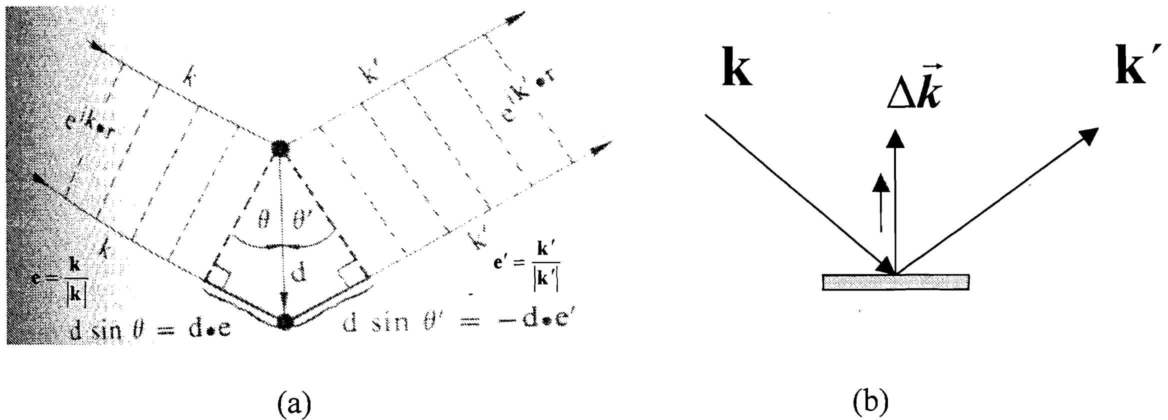

Figure 9 (a) Diffraction schematic in k-space, where ***k*** is a wave vector. (b) Diagram of ***k, k', and*** Δk relation and orientation in a theta/2theta scan.

The $\theta/2\theta$ scan identifies peaks at the detector k_f for Δk values satisfying the Laue diffraction condition, that $\Delta k \in G$, where G is the reciprocal lattice.

4.2.2 XRD concentration calculation

In hexagonal systems, the interplanar spacing d can be expressed as [18]:

$$\frac{1}{d^2} = \frac{4}{3}\frac{h^2 + hk + k^2}{a^2} + \frac{l^2}{c^2} \tag{63}$$

where d is the distance in between adjacent planes, (h,k,l) are plane's coordinates in the crystal lattice, and a and c are the lattice constants of the hexagonal structure.

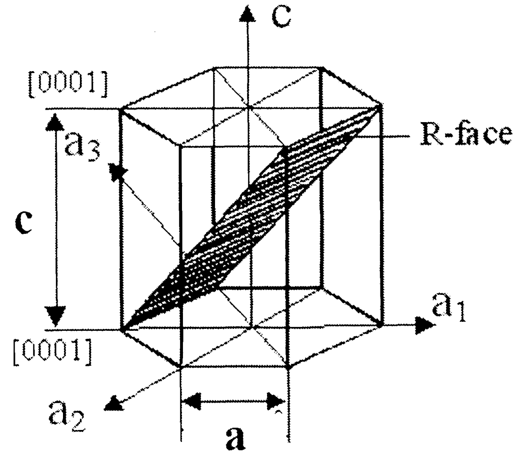

Figure 10. Hexagonal wurtzite structure and surface planes

In the wurtzite structure, shown in Figure 10, there are four symmetry directions along the a_1, a_2, a_3, and c axes. The corresponding Miller indices (h,k,j,l) are the whole number ratios relating the values along these axes. Utilizing the hexagonal symmetry of the base, $j=-(h+k)$, and the Miller indices may be reduced to (h,k,l).

Since the structure we are considering is wurtzite along the [0001] direction, the spacing between the planes will be the lattice constant c. From Bragg's law, we have

$$d\sin\theta = n\lambda \tag{64}$$

where $d = c$ in the [0001] direction, $n = 1$ for the first order of diffraction, and λ is the wavelength of the x-rays. In our case, the x-rays radiated from a Cu target had a wavelength $\lambda = 1.54\text{Å}$ (κ_α line). We assign a separate equation for GaN and AlN.

$$\begin{aligned} d_{GaN}\sin\theta_{GaN} &= n\lambda \\ d_{AlN}\sin\theta_{AlN} &= n\lambda \end{aligned} \quad \text{for } n = 1 \tag{65}$$

Applying given lattice constants in the c direction: $c_{GaN} = 5.185$, and $c_{AlN} = 4.982$, gives the resulting diffraction angles without error for first order diffraction:

$$\sin\theta_{GaN} = \frac{1.54}{5.185} \Rightarrow \theta_{GaN} = 17.278^\circ$$
$$\sin\theta_{AlN} = \frac{1.54}{4.982} \Rightarrow \theta_{AlN} = 18.006^\circ \quad (66)$$

$$\therefore \theta_{AlN} - \theta_{GaN} = 0.728^\circ$$

The procedure that we followed to determine the composition of the AlGaN layers from XRD data will be shown for sample #2036. Figure 11 is a logarithmic experimental XRD data plot, fit with two Gaussian curves. The two peaks correspond to GaN and AlGaN.

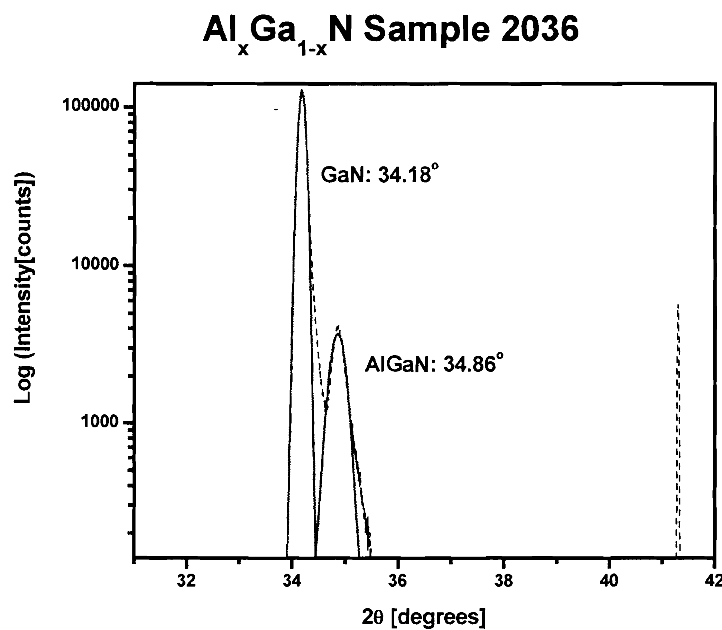

Figure 11. A sample XRD logarithmic data spectra and fit with parameters.

Due to small calibration imperfections, we first calculated the shift in all angle measurements from a reference point. For reference, we used the ideal GaN peak location from (66) with the fit results for the first peak. From this point, an asterisk (*) denotes experimental data.

$$2\theta^{*}_{GaN} = 34.180^{\circ}$$
$$\theta^{*}_{GaN} = 17.090^{\circ} \tag{67}$$
$$\theta_{shift} = \Delta\theta = \theta_{GaN} - \theta^{*}_{GaN} = 0.188$$

Accounting for the shift, the diffraction angle for this $Al_xGa_{1-x}N$ sample was found to be 17.620 degrees.

$$\theta^{*}_{AlGaN} = \frac{34.863}{2} + \theta_{shift} = 17.620^{\circ} \tag{68}$$

Using Bragg's law (64), the lattice constant for the sample $d_{2036} = c$ may be calculated for the first order diffraction, with $\lambda = 1.54$Å:

$$c_{2036}\sin(\theta^{*}_{AlGaN}) = 1.54\,\text{Å}$$
$$c_{2036} = \frac{1.54}{\sin(17.620)} = 5.088\,\text{Å} \tag{69}$$

By Vegard's Law, stated specifically for $Al_xGa_{1-x}N$ in (70), the lattice constants are linearly related to the alloy concentration. Using the known lattice constants, we arrive at the concentration of Al (x) in the sample.

$$c_{Al_xGa_{1-x}N} = c_{AlN}x + (1-x)c_{GaN} \tag{70}$$

$$x = \frac{c_{AlGaN} - c_{GaN}}{c_{AlN} - c_{GaN}}$$
$$x = \frac{5.088 - 5.185}{4.982 - 5.185} = 0.480 \tag{71}$$

Sample 2036 is 48% aluminum at the point of the XRD measurement. Similarly, we calculated the other sample alloy concentrations.

4.2.3 An alternate method

In literature, a common approximation used in determining concentration from XRD spectra is to assume $\sin\theta$ is linear if the considered angle range is small.

This method begins by assuming the linear relation between the alloy concentration and the lattice constants in Vergard's Law, and rearranging as in (71). If we substitute Bragg's law for $n = 1$ into equation (71):

$$x = \frac{\dfrac{\lambda}{\sin\theta_{AlGaN}^{*}} - \dfrac{\lambda}{\sin\theta_{GaN}^{*}}}{\dfrac{\lambda}{\sin\theta_{AlN}} - \dfrac{\lambda}{\sin\theta_{GaN}}} \tag{72}$$

This simplifies to the form:

$$x = \left(\frac{\sin\theta_{AlN}}{\sin\theta_{GaN}}\right)\left(\frac{\sin\theta_{GaN}^{*} - \sin\theta_{AlGaN}^{*}}{\sin\theta_{GaN} - \sin\theta_{AlN}}\right) \tag{73}$$

Assuming $\sin\theta$ is linear in the range under consideration the ternary alloy concentration is proportional to ratio involving the angles themselves:

$$x = \left(\frac{\theta_{AlN}^{*}}{\theta_{GaN}^{*}}\right)\left(\frac{\theta_{GaN}^{*} - \theta_{AlGaN}^{*}}{\theta_{GaN} - \theta_{AlN}}\right) \tag{74}$$

The asterisk (*) indicates experimental XRD data, derived from the same Gaussian fit results as used in the previous concentration calculation.

4.3 Contactless Electroreflectance Experimental Setup

Electromodulation can be performed without contacts and sample destruction during contactless electroreflectance (CER) experiments. CER uses a capacitor-like arrangement around the sample, and a modulating high voltage between the capacitor plates. **Figure 12** illustrates the setup used in this thesis.

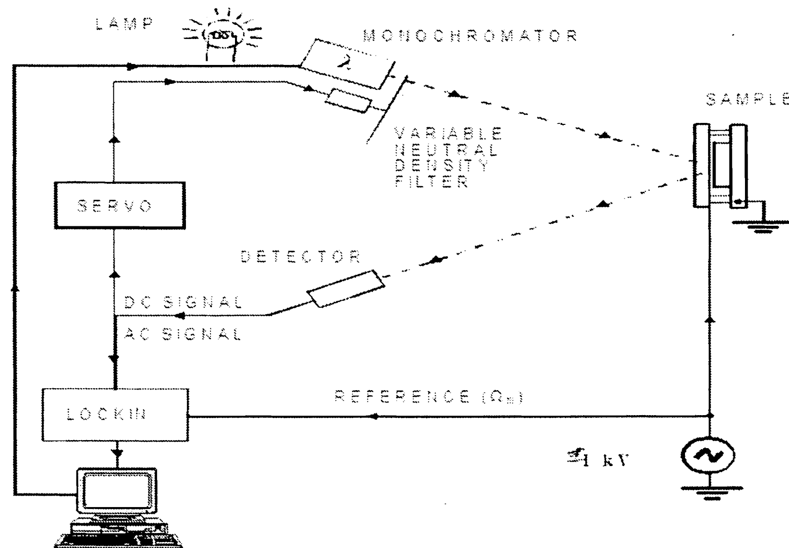

Figure 12 CER set up.

Throughout the scan, the modulating electric field about the sample is applied between the plates of the capacitor. This electric field is generated by applying high voltage between the capacitor plates, which were the Al holder and a wire grid. The high voltage is produced by passing a TTL reference signal through a high voltage amplifier, Trek model 609E-6. The TTL reference signal is generated by a Signal Recovery EG&G lock-in amplifier model 7265 at a frequency set to 1-3 kilohertz (kHz). The magnitude of the high voltage generated by the Trek amplifier is around 1 kilovolt (1kV peak to peak).

The sample is attached to the holder (shown in **Figure 13**) with rubber cement. The wire grid, mounted on a plastic insulator, is held about one millimeter (1mm) from the surface of the sample.

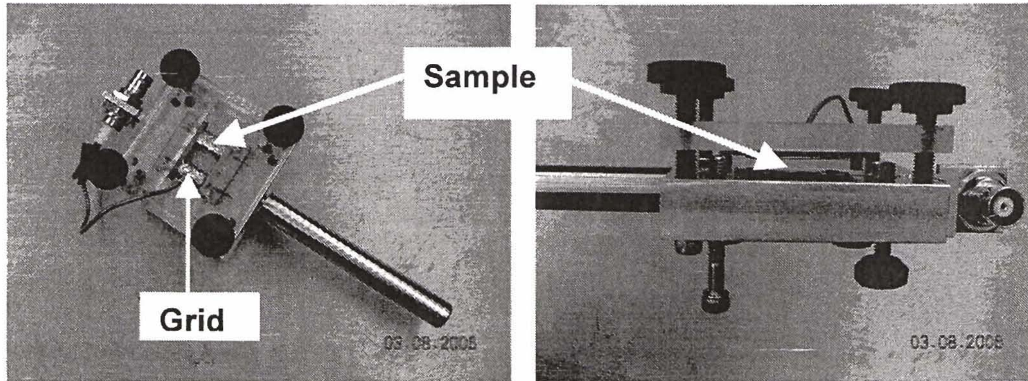

Figure 13. CER sample holder.

A 150W xenon compact arc lamp, set to 135W during experimental runs, is powered by the lamp power supply model LPS-220B from Photon Technology, Inc. (PTI). Light from the lamp is controlled by PTI's model 101 monochromator, and a variable neutral density filter (VNDF) of our group's own construction The Hamamatsu model H5784-03 solid state photomultiplier detector in our set up has a wavelength range between 185 nm and 650 nm, or energy range of 1.9eV to 6.7eV. The lock-in serves to control and record only the signal data coming in from the detector. The detector sends a mixture of direct (dc) and alternating current (ac) signals to the lock-in, which splits them assigning:

$$\begin{aligned} dc &= I(\lambda)R(\lambda) = c \\ ac &= I(\lambda)\Delta R(\lambda) = c\frac{\Delta R(\lambda)}{R(\lambda)} \end{aligned} \tag{75}$$

As previously mentioned, the d.c. is held constant using the VNDF.

4.4 Data Acquisition (DAQ)

The computer's data acquisition program is WinPR. The program was previously developed by Dr. Muñoz and his co-workers. A menu screen with sample settings is shown below in **Figure 14**.

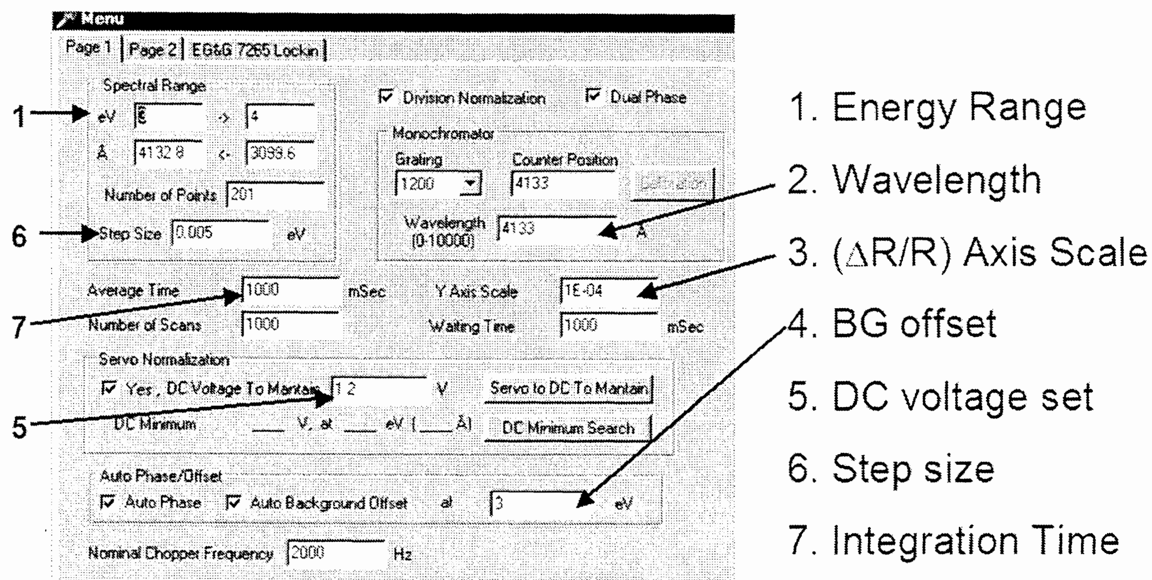

Figure 14. Data acquisition menu in WinPR.

The spectral range box (item 1 in **Figure 14**) was set according to the desired energy range. Item 2 displays the current wavelength of the monochromator. Signal intensity was on the order of 10^{-5} to 10^{-4}, so the Y-Axis scale (item 3) was set accordingly. Item 4, the background offset, adjusts the signal to zero for the energy value selected, typically the initial scan energy set in item 1. Item 5 defines the DC voltage value for the servo normalization. Customarily, the step size (item 6) was set to 5meV resolution for a rough transition identification, then to 2meV for higher resolution of the transition energy. For noise reduction, the number of scans ranged from 40 to 80. The integration time (item 7) sets the time the computer reads the incoming lock-in data. WinPR ultimately plots $\frac{\Delta R(\lambda)}{R(\lambda)}$, calculated using the dc and ac signals that are the results of the experimental set up (equation (75)), vs. Energy (eV).

4.5 CER Results and Analysis

The A excitonic transition as a function of alloy concentration in $Al_xGa_{1-x}N$ has been previously studied using several techniques, such as optical absorption [19-22], transmission [23], reflection [11,24], photoreflectance (PR) [25], and photoluminescence (PL) [11,26,27]. However, the results are controversial with respect to the bowing parameter b, which defines the Al concentration x effect on the band gap energy, in the established equation (76):

$$E_g^{AlGaN} = xE_g^{AlN} + (1-x)E_g^{GaN} - bx(1-x). \tag{76}$$

Reports include a positive (downward), negative (upward), and zero (linear) bowing parameter b. Figure 15 illustrates twenty-eight separate band gap measurements as a function of alloy concentrations from different sources [11]. The results are plotted so the deviation of the bowing parameter from zero (linear) is apparent.

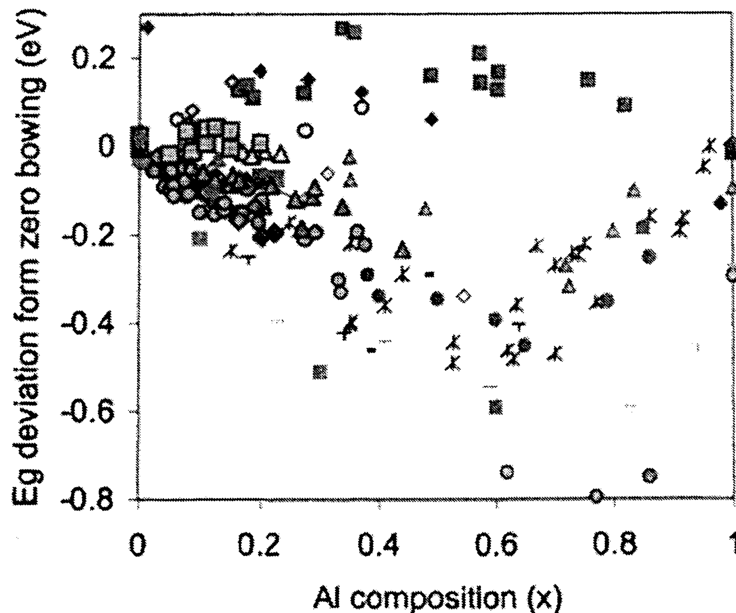

Figure 15 Experimental data from published works of Al composition in AlGaN versus energy band gap plotted as the deviation from zero bowing [11]

It is obvious a consensus has hardly been reached regarding this parameter. The majority of the works citing a non-zero bowing parameter propose a positive b value, corresponding to a negative deviation from linearity.

Figure 16 contains the CER spectra and their corresponding fits in dashed and solid lines, respectively.

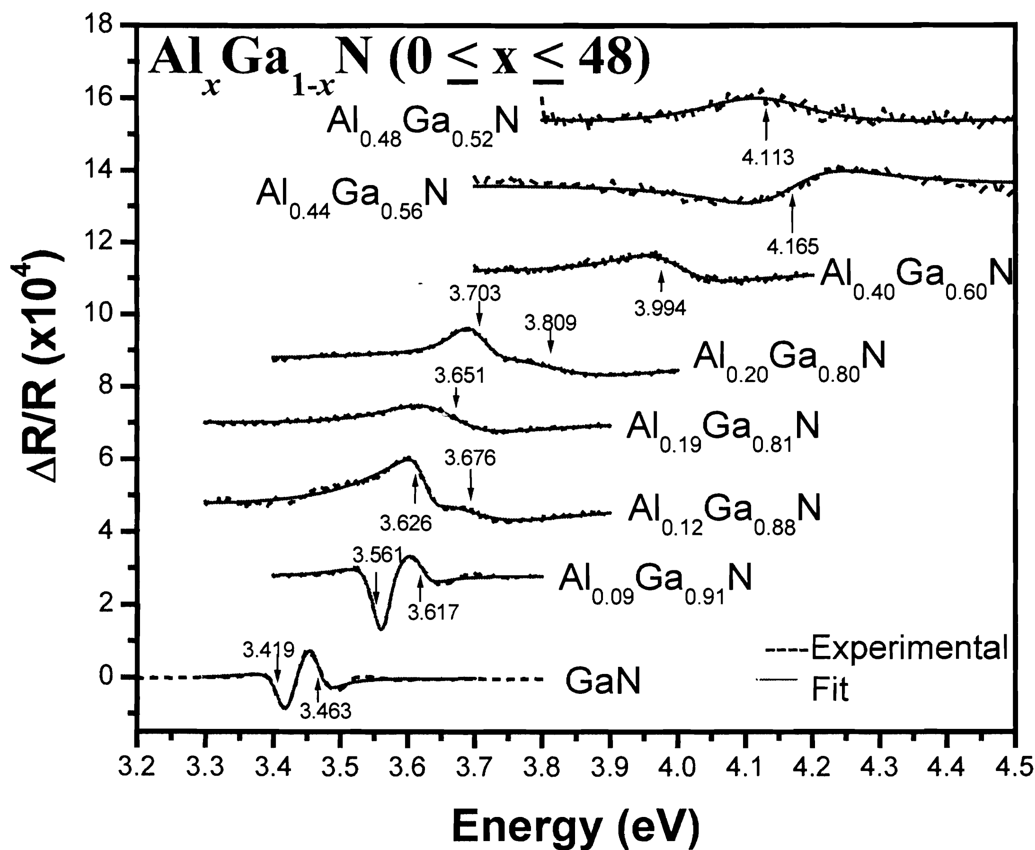

Figure 16 *CER spectra of $Al_xGa_{1-x}N$ for $0 \leq x \leq 0.48$*

The fitting was performed in the WinPR program. Lorentzian line shapes were used to fit the function described in the lineshape considerations section 3.2.4, with $m = 2$. The fit parameters for each feature were the amplitude, broadening parameter, phase, and band

gap energy. The program allowed for fixed and variable setting for each parameter. Figure 17 shows the band structure of a III-Nitride semiconductor around the Γ point. This figure illustrates that the three lowest energy transitions correspond to excitons A, B, and C, respectively.

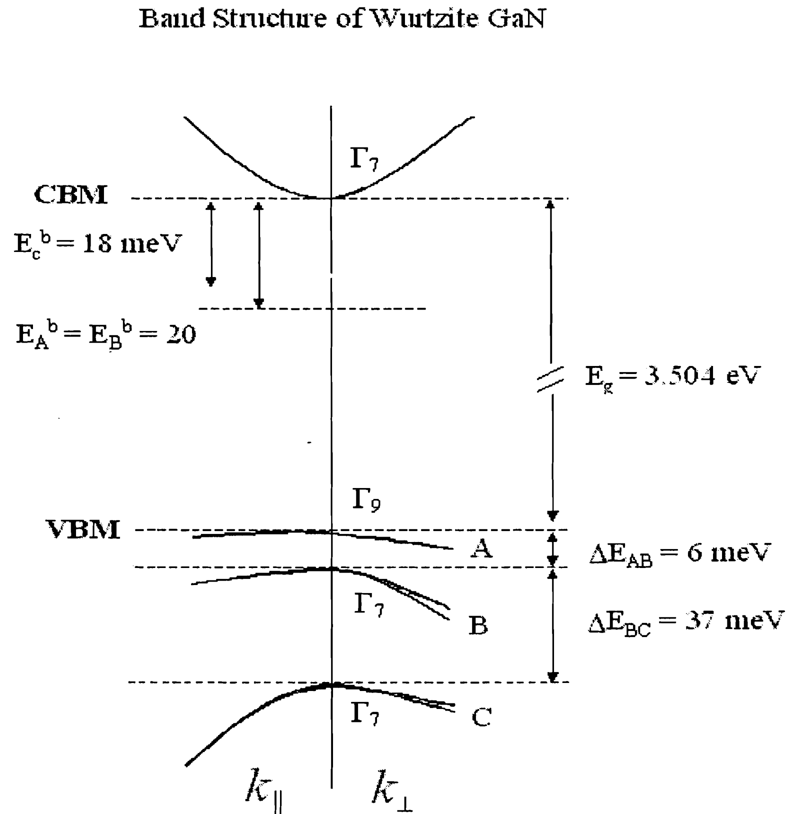

Figure 17. Band structure of Wurtzite GaN.

According to the polarization selection rules, the A and B transitions are allowed for light ***E*** polarization perpendicular to the c-axis. The C transition is allowed for ***E*** parallel to the c-axis. Because the layers have their c-axis normal to the substrate plane, $\boldsymbol{E} \perp \boldsymbol{c}$ is predominantly obtained, leading to dominant A and B transitions in the spectra. The presence of the C transition in the spectra is due to depoloarization originating from strain present in the material [34]. The B and C excitons have characteristically and

comparatively weaker intensities, and their signals become broader at increased temperatures due to increasing oscillator strength. Figure 16 shows the low and high energy transitions correspond to the A and C excitons, respectively.

Table 1 lists the results obtained from Figure 16. We incorporated a previously reported value for the band gap of AlN [28] into our data.

Al concentration	**A-exciton energy (eV)**	**C-exciton energy (eV)**
0	3.419	3.463
0.09	3.561	3.617
0.115	3.626	3.676
0.19	3.651	*not detectable*
0.205	3.703	3.809
0.4	3.994	*not detectable*
0.44	4.165	*not detectable*
0.48	4.113	*not detectable*
1	5.94	*n/a*

Table 1. Al concentration XRD measurements and corresponding A-exciton CER energy measurements

Over the entire composition range, the fundamental exitonic transition, E_A, as a function of alloy concentration, can be described by a quadratic polynomial fit shown below in Figure 18 given by:

$$E_A^{AlGaN} = 3.419 + 0.852x + 1.7x^2 \tag{77}$$

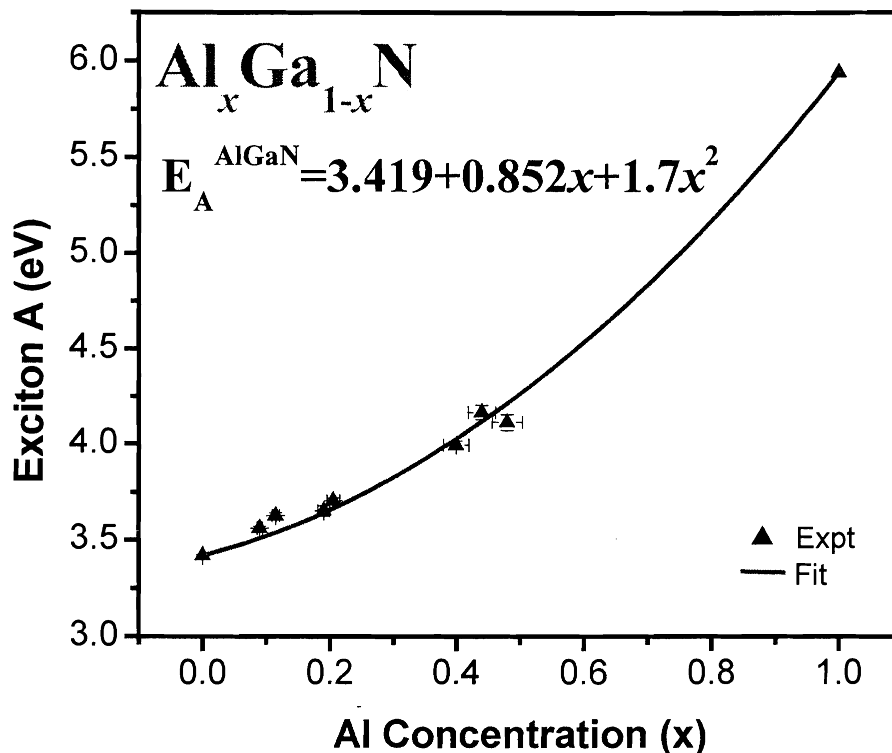

Figure 18. Effect of Al concentration on the A excitonic transition of $Al_xGa_{1-x}N$.

The error bars displayed account for 5% of the Al concentration measurement error either way ($x \pm 0.05x$). Error in excitonic energy was assumed to be one quarter of the signal width either way. Our bowing parameter b = 1.7 eV falls towards the higher end of the cited range of $-0.8eV \leq b \leq 2.6eV$. The measurements for the higher Al concentration samples are seen to drive the bowing parameter most, yet have the largest error regions. It is notable the CER spectra become broader with increasing Al concentration. This is an indication of non-uniformity in the sample. Interstitial Al atoms and clusters give rise to local strain. It has also been suggested this higher bowing parameter may be explained by composition disorder. Larger bandgap differences between the composite alloys cause larger potential perturbations. If the main contribution to bowing is the composition

disorder, the bowing parameter is expected to increase accordingly [29, 30]. For comparison, the InGaN bowing parameter has been reported as 1.43 eV [31].

If we consider the samples measured by CER in the concentration range of zero to forty-eight percent aluminum concentration, $0 \le x \le 0.48$, we find a linear shown in Figure 19, and given as

$$E_A^{AlGaN} = 3.419 + 1.51x \tag{78}$$

This is in agreement with numerous sources [22, 25, 27]. However, all cite linearity (a zero bowing parameter) for ranges of samples with low aluminum concentration $x \le 0.4$.

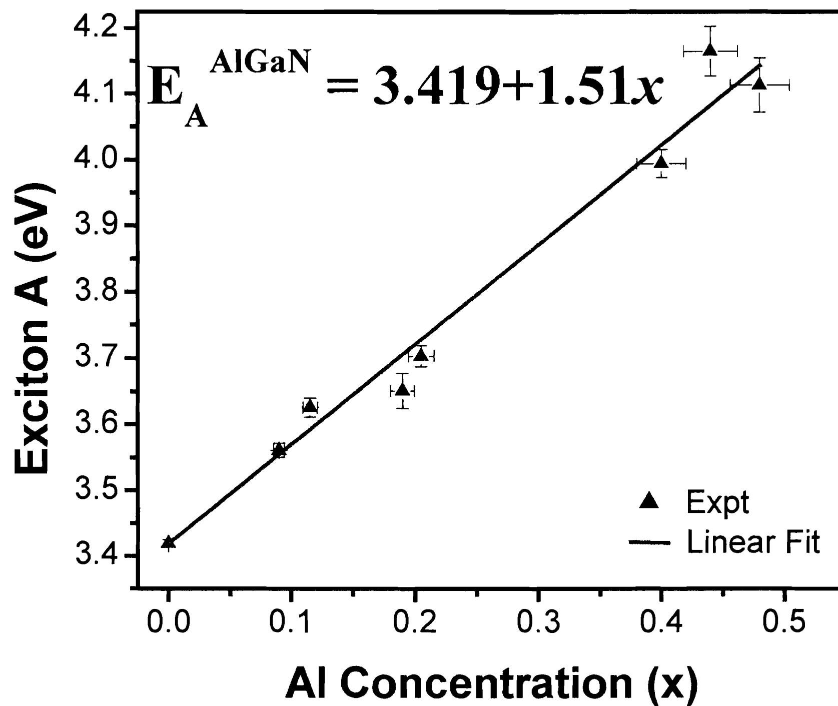

Figure 19. Effect of Al concentration on the A excitonic transition of $Al_xGa_{1-x}N$.

In addition, for the detectable C exciton transitions, it is notable a linear trend-line with a similar slope to (78) fits the data well, as shown in Figure 20, and given by

$$E_C^{AlGaN} = 3.467 + 1.70x \quad (79)$$

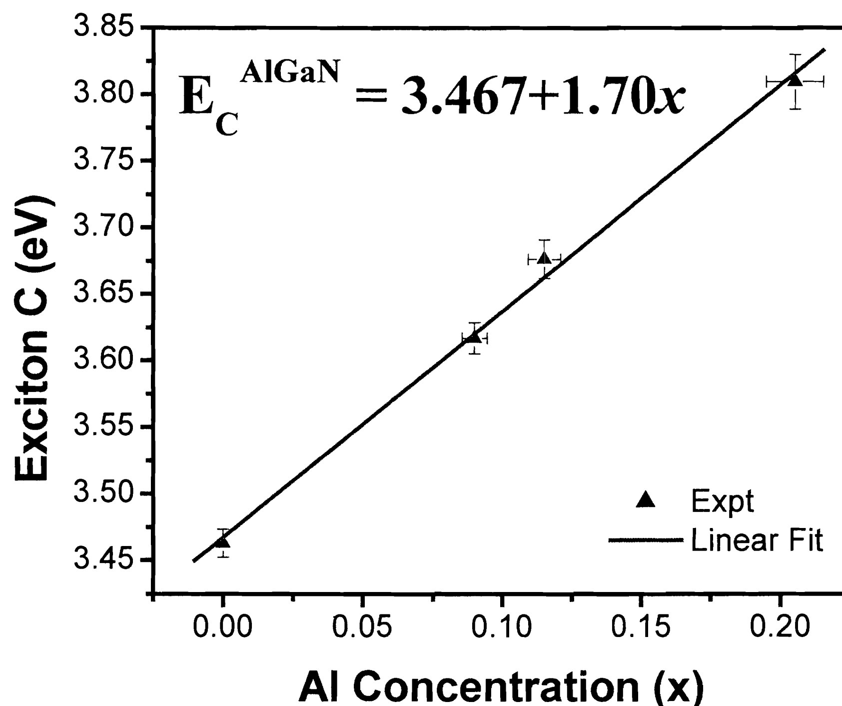

Figure 20. Effect of Al concentration on the C excitonic transition of $Al_xGa_{1-x}N$

It has also been shown that strain [32,33] and temperature [34] significantly effect the energy gap value. The effect of strain as a function of the layer thickness specific to $Al_xGa_{1-x}N$ is presented in reference [35]. Temperature dependence specific to $Al_xGa_{1-x}N$ can be found in reference [36].

One of the main problems we found in this work was the determination of the composition by XRD. Non-uniformity throughout the sample may result in composition changes across the sample. If XRD measurements were taken in a different location than the CER measurements, transition energies would be erroneously paired with aluminum concentrations. $Al_xGa_{1-x}N$ is difficult to grow at high Al concentrations due to lattice

mismatch. As such, the uncertainty of concentration measurements becomes greater. As can be seen in Figure 18, the trend line underestimates energy transitions of lower Al concentration samples. Assuming less composition uncertainty (more uniform growth), we see the bowing would be slightly less.

Despite this uncertainty, this work has furnished experimental results that extend beyond typical Al concentration range for room temperature measurements [20, 21, 23, 24-26]. We have also successfully utilized CER, a technique that has not been used to analyze Al concentration effects on $Al_xGa_{1-x}N$ excitonic transitions, yet provides superior resolution.

Chapter 5. Conclusions

It has been shown CER is a viable and accurate method in the study of band gaps and exciton transitions. Its high resolution at room temperature places it at the forefront of optical techniques in terms of desirable experimental traits.

Using a previously reported A-excitonic energy for AlN [28] and CER spectra of samples ranging in Al concentration for $0 \leq x \leq 0.48$, our study resulted in a bowing parameter b = 1.7 eV for the A exciton over the entire aluminum composition range ($0 \leq x \leq 1$). This is within the reported range of $-0.8 \leq b \leq 2.6$, although includes data for comparatively high aluminum concentration samples at room temperature. Restricting the fit to $0 \leq x \leq 0.48$ concentration, the range of our CER spectra, we found a linear fit ($E_A^{AlGaN} = 3.419 + 1.51x$) was able to describe the behavior. The same was true of the trendline ($E_C^{AlGaN} = 3.467 + 1.70x$) through the detectable C exciton transitions as a function of the composition.

Sample quality has been an obstacle, as it is difficult to produce highly uniform samples of $Al_xGa_{1-x}N$ with high aluminum concentration. The lattice mismatch and non-uniformity account for inaccuracies in composition determination. Stress dependence may skew energetic results.

References

1. "Blu-ray and HD DVD blitz Vegas show" *Compound Semiconductor*. **12**. No. 1. p. 5. January/February (2006).

2. T. Maeda, M. Terao, and T.Shimano, "A review of optical disk systems with blue-violet laser pickups", *Japanese J. Appl. Phys Part 1, **42,** 1044 (2003).*

3. H. Morkoç, *Nitride Semiconductors and Devices*, Second edition, Springer 2006.

4. M. Kneissl, D. W. Treat, M. Teepe, N. Miyashita, and N. M. Johnson, "Ultraviolet AlGaN multiple-quantum-well laser diodes", *App. Phys. Lett. **82,** 4441 (2003).*

5. S. Nakamura, S. Pearton, and G. Fasol, *The blue laser diode: the complete story* ; Springer, Berlin 2000.

6. R. M. A. Azzam and N.M Bashara. *Ellipsometry and Polarized Light.* North-Holland Publishing Company. (1977)

7. Q.S. Paduano, D.W. Weyburne, L.O. Bouthillette, S. Wang, and M.N. Alexander. Jpn. J. Appl. Phys. **41**. Part 1, No. 4A. (2002)

8. B. Gil. Nanotechnology **12**. (2001).

9. E.D. Palik. *Handbook of Optical Constants of Solids*. Vol. 1. Academic Press. (1985).

10. M. Muñoz , Y.S. Huang, F.H. Pollak, and H. Yang. J. Appl. Phys. **93.** No. 5. (2003).

11. F. Yun, M.A. Reshchikov, L. He, T. King, H. Morkoç, S.W. Novak, and L. Wei. J. Appl. Phys. **92**, 4837- (2002).

12. P. Yu and M. Cardona. *Fundamentals of Semiconductors: Physics and Materials Properties.* Springer. (2005).

13. J.D. Jackson. *Classical Electrodynamics*, 2nd edn. Wiley, New York. (1975).

14. L.D. Landau and E.M. Lifshitz, *Quantum Mechanics.* 3rd edn. Pergarmon Press. (1977)

15. N. W. Ashcroft and N. D. Mermin, *Solid State Physics*, Thomas Learnin, Inc. (1976).

16. E. Butkov, *Mathematical Physics.* chapter 6.4. Addison-Wesley Publishing Company. (1966).

17. O.J. Glembocki and B.V. Shanabrook, *Semiconductors and Semimetals.* **36**, editors D.G. Seiler and C.L. Littler. Academic Press (1992).

18. B.D. Cullity, *Elements of X-Ray Diffraction, 2nd edition.* Addison-Wesley Publishing Company, Inc. (1978).

19. J. Hagen, R.D. Metcalfe, D. Wickenden, and W. Clark, J. Phys. C: Solid State Phys.,

11, 143-146 (1978).

20. S. Yoshida, S. Misawa, and S. Gonda, J. Appl. Phys. **53**, 6844-6848 (1982).

21. Y. Koide, H. Itoh, M.R.H. Khan, K. Hiramatu, N. Sawaki, and I. Akasaki, J. Appl. Phys. **61**, 4540 (1987).

22. D.K. Wickenden, C.B. Bargeron, W. A. Bryden, J. Miragliotta, and T.J. Kistenmacher, Appl. Phys. Lett. **65**, 2024 (1994).

23. M.A. Khan, R.A. Skogman, R.G. Schultze, and M. Gershenzon, Appl. Phys. Lett. **43**, 492-494 (1983).

24. H. Jiang, G. Y. Zhao, H. Ishikawa, T. Egawa, T. Jimbo, and M. Umeno, J. Appl. Phys. **89**, 1046 (2001).

25. T.J. Ochalski, B. Gil, P. Lefebvre, N. Grandjean, M Leroux, J. Massies, S. Nakamura, and H. Morkoç, Appl. Phys. Lett. **74**, 3353 (1999).

26. S.R. Lee, A.F. Wright, M. H. Crwford, G.A. Petersen, J. Han, and R.M. Biefeld, Appl. Phys. Lett. **74**, 3344 (1999).

27. M.R.H. Kahn, Y. Koide, H. Itoh, N. Sawaki, and I. Akasaki, Solid State Commun. **60**, 509 (1986).

28. E. Silveira, J.A. Freitas, Jr., M. Kneissl, D.W. Treat, N.M. Johnson, G.A. Slack, and L.J. Schowalter, Appl. Phys. Lett., **84**, No. 18 (2004).

29. J. Wu, W. Walukiewicz, K.M. Yu, J.W. Ager III, S.X. Li, E.E. Haller, H. Lu, W.J. Schaff, Universal Bandgap Bowing in Group III Nitride Alloys, Solid State Communications, **127** (2003).

30. J.A. Van Vechten and T.K. Bergstresser. Phys. Rev. B. **1**, No. 8. (1970).

31. J. Wu, et. al., Appl. Phys. Lett., **67**, 1745. (2002).

32. G. Steude, B.K. Meyer, A. Goldner, A. Hoffman, A. Kaschner, G Bechstedt, H. Amano, and I. Akasaki. Jpn. J. Appl. Phys. **38**. Pt.2, No. 5A (1999).

33. F.H. Pollak, *Semiconductors and Semimetals, Vol. 55*, Chapter 4: Effects of External Uniaxial Stress on the Optical Properties of Semiconductors and Semiconductor Microstructures. Academic Press. (1998).

34. B. Gil, ed., F. H. Pollak, *Group III Nitrides Semiconductor Compounds: Physics and Applications.* Chapter 5: Modulation spectroscopy of the Group III Nitrides. Clarendon Press. Oxford. (1998).

35. O. Katz, B. Meyler, U. Tisch, and J. Salzman, Phys. Stat. Sol. (a) **188**. No. 2 (2001).

36. D. Brunner, H. Angerer, E. Bustarret, F. Freudenberg, R. Höpler, R. Dimitrov. J. Appl. Phys. **82**, 10, (1997).

Appendix A

High Voltage Amplifier & Lock In

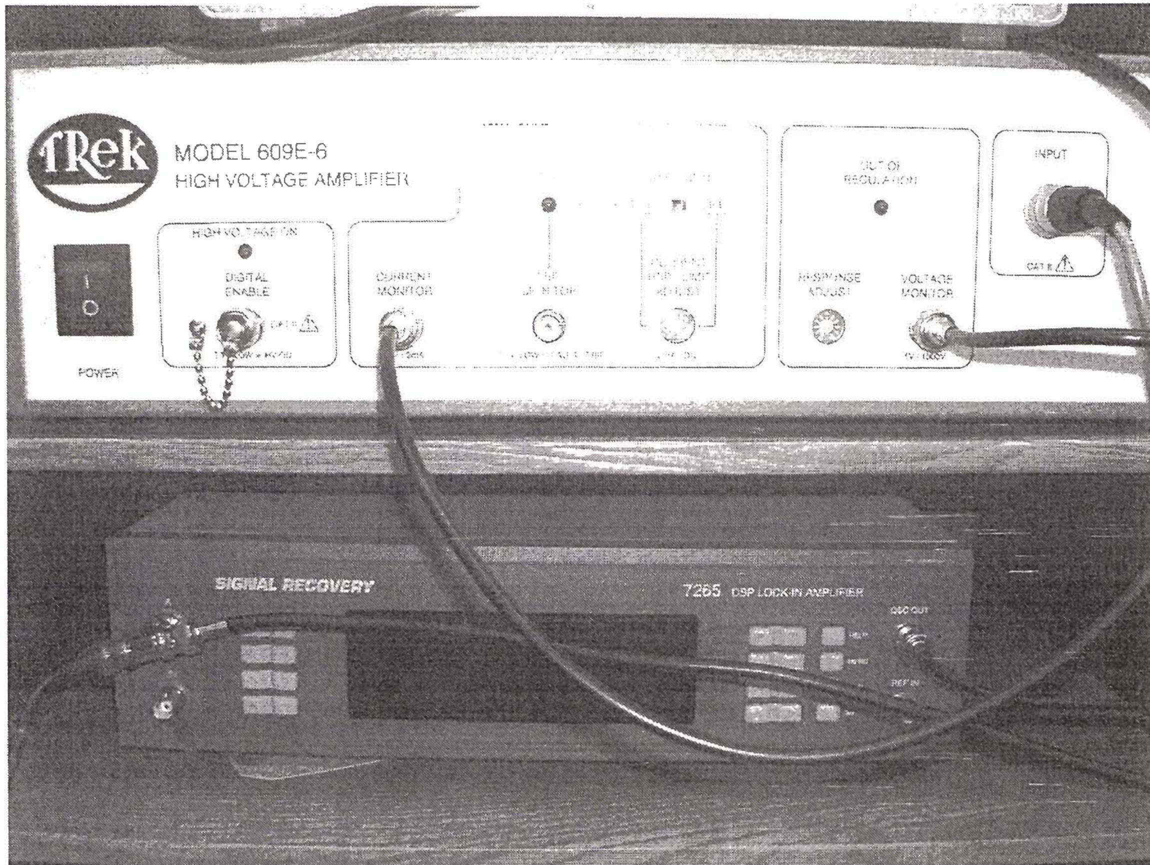

High Voltage Amplifier settings:

- Current Trip/Limit Adjust: 10
- Response Adjust: 0

Vita

Laura Christine McGlinchey was born November 19, 1978 in Pusan, South Korea. Following her adoption at three months old, she became a US citizen. Laura's primary and secondary education was in the Philadelphia Catholic Schools system. Through a University Scholarship, she was able to attend the University of Richmond in Richmond, Virginia, where she earned a B.S. in Mathematics, a B.A. in Physics, and a minor in secondary education. Throughout her undergraduate years, she was involved in experimental particle physics research conducted at Jefferson National Accelerator Facility. Upon graduation, Ms. McGlinchey was hired by Henrico County Public Schools and taught physics and math at Douglas S. Freeman High School for four years before deciding to pursue a master's degree. In May 2006, she successfully completed her M.S. in Physics at Virginia Commonwealth University in Richmond, Virginia. She looks forward to returning to the high school classroom, with the goal of reforming science education in the United States.